PULSE-ECHO IMAGE FORMATION USING NONQUADRATIC REGULARIZATION WITH SPECKLE-BASED IMAGES

BY

ROBERTO JANNIEL LAVARELLO MONTERO

Ingeniero Electrónico, Pontificia Universidad Católica del Peru, 2002

THESIS

Submitted in partial fulfillment of the requirements
for the degree of Master of Science in Electrical Engineering
in the Graduate College of the
University of Illinois at Urbana-Champaign, 2005

Urbana, Illinois

To Kely, my family, and friends.

ACKNOWLEDGMENTS

There are many people to which I would like to thank: my adviser, Professor William O'Brien Jr., for helping me with many useful comments and ideas but also for demanding my best effort in everything that I do and helping me to challenge myself every step of the way. Professor Farzad Kamalabadi, who provided very interesting and useful discussions about regularization methods and image processing issues and encouraged me to accomplish the best possible work. It has been a privilege to work with such outstanding researchers. All the people at the Bioacoustics Research Laboratory (BRL), the finest group that I have ever had the pleasure to work with. I thank my friends and family —César, Maria Luisa, Carmen and Pammela— for being there always for me and caring about me the way that they do. And finally, to my beloved Kely. She is the greatest joy in my life, and her love and support always motivates me to accomplish my goals.

TABLE OF CONTENTS

LIST OF ABBREVIATIONS vii

CHAPTER 1 INTRODUCTION 1
1.1 Conventional Ultrasonic Imaging Approaches 1
1.2 Inverse Problems Approach to Ultrasonic Imaging 5
1.3 Contribution of this Work 7
1.4 Organization of this Thesis 7

CHAPTER 2 CONVENTIONAL ULTRASONIC IMAGING 8
2.1 B-Mode Imaging 8
2.1.1 Two-point spatial resolution of a B-mode imaging system . . . 8
2.1.2 Characteristics of common geometries for ultrasonic transducers 10
2.2 Stripmap Synthetic Aperture 13
2.2.1 SAFT signal processing for stripmap configuration 14
2.2.2 Spatial resolution of stripmap synthetic aperture techniques . 16

CHAPTER 3 REGULARIZATION THEORY FOR IMAGE RECONSTRUCTION 19
3.1 Pulse-Echo Imaging Problem Using an Inverse Problems Formulation 19
3.2 Least Squares and Generalized Solution 22
3.3 Regularization 23
3.4 TSVD Regularization 24
3.5 Tikhonov Regularization 25
3.6 Generalized Tikhonov Regularization 26
3.7 Automatic Regularization Parameter Selection Techniques 28

CHAPTER 4 SIMULATIONS 32
4.1 Choice of the Regularization Parameters 36
4.1.1 Choice of regularization matrix L 36

4.1.2 Choice of the offset parameter β 36
4.1.3 Choice of the regularization cost norm k 37
4.1.4 Choice of the regularization parameter α 38
4.2 Effect of the Bandwidth of the Transducer 41
4.3 Effect of the Focal Number of the Transducer 46
4.4 Effect of the Distance of the ROI to the Focus of the Transducer . . . 50

CHAPTER 5 CONCLUSIONS AND FUTURE WORK 57
5.1 Conclusions 57
5.2 Future Work 58
5.2.1 Statistical analysis of the problem 58
5.2.2 Changes in the simulation setup 58
5.2.3 Changes in the reconstruction algorithm 59
5.2.4 Effect of the grid 59
5.2.5 Matrix-free solution to the problem 60
5.2.6 Changes in the forward model 60

REFERENCES 61

LIST OF ABBREVIATIONS

GCV : Generalized cross validation

MMSE : Minimum mean square error

MSE : Mean square error

NDE : Nondestructive evaluation

PRF : Pulse repetition frequency

PSF : Point spread function

ROC : Radius of curvature

ROI : Region of interest

SAFT : Synthetic aperture focusing techniques

SNR : Signal-to-noise ratio

SVD : Singular value decomposition

TSVD : Truncated singular value decomposition

CHAPTER 1

INTRODUCTION

1.1 Conventional Ultrasonic Imaging Approaches

The use of acoustic waves for imaging purposes goes back to the 1910s when Paul Lavengin demonstrated the use of the sound navigation ranging (sonar) method [1]. The key concept for acoustic imaging is that an acoustic wave propagating through a medium is scattered when inhomogeneities are encountered. Thus, inhomogeneities inside a volume can be detected by radiating it with an acoustic wave and measuring the scattered energy with sensors located in different locations. Nowadays, acoustic imaging is used for several applications including nondestructive evaluation (NDE) for the analysis of different materials such as concrete [2], steel [3] and even wood [4]; and biomedical imaging for intravascular [5] and dermatological [6] applications and for cancer detection [7], among many others [8].

Acoustic imaging systems use transducers, devices capable of both transmission and reception of acoustic waves. On the simplest configuration, a single-element transducer is placed at a certain position, on which it transmits an acoustic wave and then receives the backscattered echoes. This imaging modality is known as monostatic pulse-echo imaging.

Because a transducer has a finite size, the radiation pattern suffers from diffractional effects. The point spread function (PSF) of the imaging system [9] is defined as the 2-D impulse response of the system, i.e., the image that would be formed if only one infinitesimal scatterer were present in a particular position in the region of interest. A typical point spread function consists on a main lobe and sidelobes. The shape and amplitude of this function determine the quality of the images that can be formed with a particular imaging system.

The quality of an acoustical imaging system is determined by two principal quantities known as spatial and contrast resolution. Spatial resolution is the ability of the system to discriminate two targets of equal amplitude that are close together.

When dealing with 2-D images, the spatial resolution is defined independently for both axes: the axial resolution is related to the ability to discriminate two targets close together on the direction of propagation of the wave and depends on the pulse duration, whereas the lateral resolution is defined for the direction transverse to the propagation of the wave and depends on the diffraction pattern of the transducer that is used. The two points will be resolved if two peaks can be discernible in the resulting image; the criterion to determine the resolvability of the peaks, however, can be arbitrarily established, which results in several definitions for spatial resolution [9]. The Rayleigh criterion, for example, is defined as the separation between two copies of the point spread function that would result on the peak of the mainlobe of one landing on the first zero of the other. Another definition is the Sparrow criterion, which is defined as the minimum separation between two copies of the point spread function for which the dip that is formed halfway from the peaks is down in intensity by a factor of two [10].

Contrast resolution is the ability to resolve two areas of different brightness on the image. Here the main limitation is the amplitude of the sidelobes of the point spread function. Consider the case of a cystic target of low reflectivity surrounded by a region of high reflectivity scatterers. When the mainlobe is over the cyst, the sidelobes are partially over the surrounding regions which do reflect the sound more efficiently, and hence it will appear that there was reflection from inside the cyst. The higher the level of the sidelobes, the more severe this phenomenon will be. If the cyst is small enough then it can be completely filled by the reflections of the surrounding regions. It should be noted that a wide mainlobe will also shadow regions of negative contrast.

In summary, a good imaging system has a very small mainlobe and sidelobes of a very low level. However, there are several factors that can affect the PSF of an acoustic imaging system.

One factor that affects the width of the mainlobe is the wavelength of the acoustic wave, which is inversely proportional to its frequency. This is why ultrasonic waves (acoustic waves with frequencies above the audible range) are used for medical imaging, where the size of the discontinuities can be in the range of micrometers or below. However, attenuation also increases with frequency [11], thus leading to one a well-known trade-off for this kind of applications: spatial resolution versus depth

of imaging.

Transducers can be constructed using different geometries to change its diffraction pattern. The first type of transducers that was used was unfocused (such as the circular piston geometry [12]) and did not have good spatial resolution at any point in the image. Soon they were replaced by spherical transducers [10], a geometry that had a radiation pattern that was focused on a small region of space called the focal region. Even though the lateral resolution is greatly improved on the focal region, it actually worsens everywhere else due to the spreading of the beam. Because a more focused transducer has a smaller focal region, for this geometry there is a tradeoff of high resolution on the focal region versus the size of the region that can be imaged.

It is clear that the key to improve the resolution of a system is to achieve focus throughout the region of interest (ROI). When using a monostatic configuration, this can be accomplished using synthetic aperture focusing techniques (SAFT), which consist of combining the received signals corresponding to different scanning positions in order to construct a synthetic beam. The problem of this type of technique is the generation of high level sidelobes which compromise the contrast resolution; this problem can be reduced using apodization at the cost of sacrificing lateral resolution [13].

The best quality acoustic images are achieved using array imaging [14], for which more than one transducer is used to transmit and receive acoustic waves. The transducers that are grouped to form the array are known as elements, and they can be arranged in one, two or three dimensions. When the elements transmit together, the overall diffraction pattern is modified and the resulting mainlobe is narrower than the one corresponding to the individual elements. A phased array is one for which the elements can be fired individually. This is especially important because it allows to focus the transmitted field on different portions of the ROI by applying appropriate delays to every element. Sidelobe levels can be controlled by apodizing the array elements. Also, because more power is transmitted into the ROI, the signal-to-noise (SNR) level of the resulting image is improved.

However, phased array imaging has its own limitations. One of them is the appearance of grating lobes, which are due to spatial aliasing, i.e., when the center-to-center spacing between adjacent elements (known as *element pitch*) that conform the array do not satisfy the Nyquist sampling criterion. Grating lobes do not exist

if the element pitch is less or equal than a wavelength if no steering is used, and less than half a wavelength if the beam is steered [12]. It should be noted, however, that for pulsed waves this condition is relaxed due to the time separation among the pulses from individual elements. Because the minimum element pitch is dependent on the wavelength, i.e., inversely dependent on the frequency, the construction of an array is more challenging as the frequency increases. The issue of crosstalking between adjacent elements also have to be considered. Additionally, the need to have separate electrical connections to fire each element individually causes the required hardware to be more complex.

Another limitation for phased arrays is the acquisition time. Multiple transmissions are needed in order to achieve focus at different depths within the ROI. The time between the initiation of consecutive transmissions is known as pulse repetition frequency (PRF). The PRF cannot be arbitrarily large because echoes corresponding to consecutive transmissions should not overlap. Because the time of arrival of the pulses depends on the speed of sound, the PRF is a fundamental limit of phased arrays. Several techniques have been proposed to overcome this limitation, among them the use of amplitude-steered arrays [15] and coded-excitation arrays [16].

The contrast resolution is particularly compromised when dealing with speckle based images [17],[18]. The resolution cell of an imaging system is defined as the area (or volume) that corresponds to the smallest resolvable detail. Because ultrasonic imaging is coherent, when there are many scatterers randomly distributed in a resolution cell, their reflections may interfere constructively or destructively, depending on their relative position to the transducer, generating spots of brightness and darkness in the image. For focused systems, these spots tend to have a size on the order of the focal region [10], and the resulting image will have a granular appearance. Speckle is very common in ultrasound medical imaging because body tissue is a semitransparent media. If the point spread function has a wide mainlobe or high level sidelobes, the spots generated by the speckle can mask regions of negative contrast. This is particularly harmful in applications such as early cancer detection.

B-mode, SAFT, and array imaging have been studied for a long time and their limitations are well documented. There exist another approach to the problem which consists in using inverse formulations and regularization theory, for which several techniques have been proposed in acoustic and similar imaging modalities such as

radar. It is of special importance to compare their performance with that which can be obtained using conventional acoustic imaging methods. Speckle-based images are proposed as targets of reconstruction because of the limitations of conventional techniques while dealing with these type of images.

1.2 Inverse Problems Approach to Ultrasonic Imaging

Inverse formulations depend on a function (forward model) that represent the measured data at the output of a system as a function of a set of variables. An inverse problem formulation consists of finding the values of the variables of the system, given the acquired data and the forward model. An example of such an approach was explored in [19] using a minimum mean square error (MMSE) inverse filter to avoid diffractional effects in ultrasound SAFT imaging. Due to instability of the forward model in the presence of noise or errors in modeling, the mere inversion of the system can lead to inaccurate results. To deal with this limitation, prior information about the data to be recovered are incorporated also in the model used for inversion. This process in known as regularization.

A well known regularization approach is the truncated singular value decomposition (TSVD), which filters the unstable eigenvalues of the forward model to achieve stability during the inversion. The number of eigenvalues to be filtered depends on the stability of the forward model and the amount of noise in the data. TSVD was explored for B-mode imaging in studies like [20] and [21]. Its main computational limitation is the need to calculate the singular value decomposition (SVD) of the forward model.

Another commonly used technique is Tikhonov regularization, which results from adding to the error function of the least square solution an extra term that is the quadratic norm of a linear transformation of the data to be recovered. The prior knowledge is introduced through an appropriate choice of the linear transformation.

Total least squares is a natural extension to the least squares solution to a linear problem, by taking into account sources of error not only on the data but also in the forward model. Lately, this technique has been explored in [22] applied to ultrasonic inverse scattering.

A very simple yet powerful extension to Tikhonov regularization corresponds to using a linear cost function with a nonquadratic norm. This concept was first used

in a technique called *total variation regularization*, which consists of using Tikhonov regularization with a discrete gradient operator and a norm equal to 1. Such a regularization technique was found to preserve edges in images better than the equivalent quadratic Tikhonov regularizer. It was used in [23] to solve for breast ulstrasonic imaging and in [24] for underground array imaging using electromagnetic pulses.

Studies with total variation regularization showed that using a norm less than 2 for the regularization cost function results in a higher enforcement of the *a priori* information. This concept can be used with any linear operator and any value of the norm of the cost function, resulting in generalized Tikhonov regularization with l_k^k norm cost functions. Examples of the use of this type of regularization for pulse-echo imaging problems are [25] applied to spotlight SAFT radar imaging and [26] for point source localization using sensor arrays. A more general framework for the selection of valid regularization cost functions for generalized Tikhonov was explored in [27]. This relates to the work of Delaney and Bresler [28] for limited angle tomography and Jarrot et al. [29] for ultrasonic elasticity imaging.

The improved performance of nonquadratic Tikhonov occurs because it causes the solution to the augmented least mean square problem to be of the form $A(x)x = y$, where the matrix operator depends on the data, and hence incorporates additional *a priori* knowledge on the inversion equations. This is also accomplished by the least squares with point-count regularization (LPCR) [30], [31] which uses an image reconstructed with a modified Wiener filter to have an approximation of regions of high energy in order to construct a cost function that penalizes solutions with high energy content. Mumphord and Shaw regularization was conceptually introduced in [32] and deals with the joint problem of estimating the unknown data and the edge field of the image so that the energy of the edge can be used as a regularization constraint, just like the energy of the whole image is used in LPCR. This approach is of special interest for segmentation problems. A nonquadratic version of the algorithm was implemented and used to reconstruct radar and ultrasonic images in [33].

Entropic regularizers (theoretical development can be found in [34] and applications to radar imaging in [35]) are designed to enforce solutions with low energy content and were found to be superior to Tikhonov regularization for the case of sparse images.

1.3 Contribution of this Work

A wide variety of regularization techniques have been suggested for pulse-echo imaging in acoustics and other coherent imaging modalities. Most have been tested with two types of images: a small collection of isolated scatterers or compact regions with a continuous, locally uniform reflectivity distribution. However, the usefulness of regularization techniques for speckle based images has not been properly explored. Given a fixed regularization inversion method, there are many factors that can affect the quality of the reconstruction, which includes imaging parameters (such as the bandwidth of the transducer), regularization parameters (which are dependent on the specific type of regularization used), and sources of noise (such as errors in modeling or additive noise on the acquired data). All of these factors have to be considered in order to evaluate the performance of the reconstruction algorithm. Because of their conceptual simplicity and reported performance, quadratic and generalized Tikhonov have been chosen as regularization techniques. The goals of this study are to explore the feasibility and effectiveness of regularization by:

1. Evaluating the quality of the reconstruction of speckle-based images as a function of imaging parameters (i.e., bandwidth of the transducer, f/number, and distance between ROI and focal region), and

2. Comparing the reconstructed images with those obtained by conventional imaging techniques, e.g., B-mode and SAFT.

1.4 Organization of this Thesis

This thesis is organized as follows: Chapter 2 presents an overview of conventional monostatic pulse-echo imaging techniques. Chapter 3 presents formulation of pulse-echo imaging using inverse formulations and an overview of regularization theory as a tool to solve this problem. Chapter 4 presents simulations to show the performance of the inversion algorithm and the effect of several parameters in the quality of the reconstruction. Finally, Chapter 5 discusses the results of this work and offers suggestions for future work.

CHAPTER 2

CONVENTIONAL ULTRASONIC IMAGING

In the following discussion, only monostatic imaging (i.e., using only one transducer for transmission/reception) will be discussed. Array imaging will not be covered in the present study.

2.1 B-Mode Imaging

The configuration for monostatic acoustical imaging is depicted in Figure 2.1(a). The transducer is placed on a certain position over the external surface of the ROI, where it sends an acoustic pulse and receives the corresponding echoes. The envelope of the signal formed by the echoes can be displayed as a function of time (or distance if the speed of sound is known) in what is known as an A-scan [36] (A stands for amplitude); an example is shown in Figure 2.1(b). The envelope is typically compressed in a logarithmic scale because of the large dynamic range of the signal. The scanning process can be repeated for different scanning positions over a certain trajectory (typically a straight line), such that information is gathered for a cross section of the ROI; a 2-D image can be formed, with each column corresponding to a scanning position. The brightness of the pixel for each column is proportional to the amplitude of the envelope of the received echoes. Such an image is known as a B-scan or B-mode image (B stands for brightness); an example is shown in Figure 2.1(c). An echo sequence is acquired for every scanning position, and every echo sequence is mapped to a column in the B-mode image.

2.1.1 Two-point spatial resolution of a B-mode imaging system

The two-point spatial resolution of an imaging system is determined by its ability to discriminate two point-like targets close together. When the image is restricted to a plane, we are concerned about the resolution in both axes, resulting in two definitions of resolution [10]:

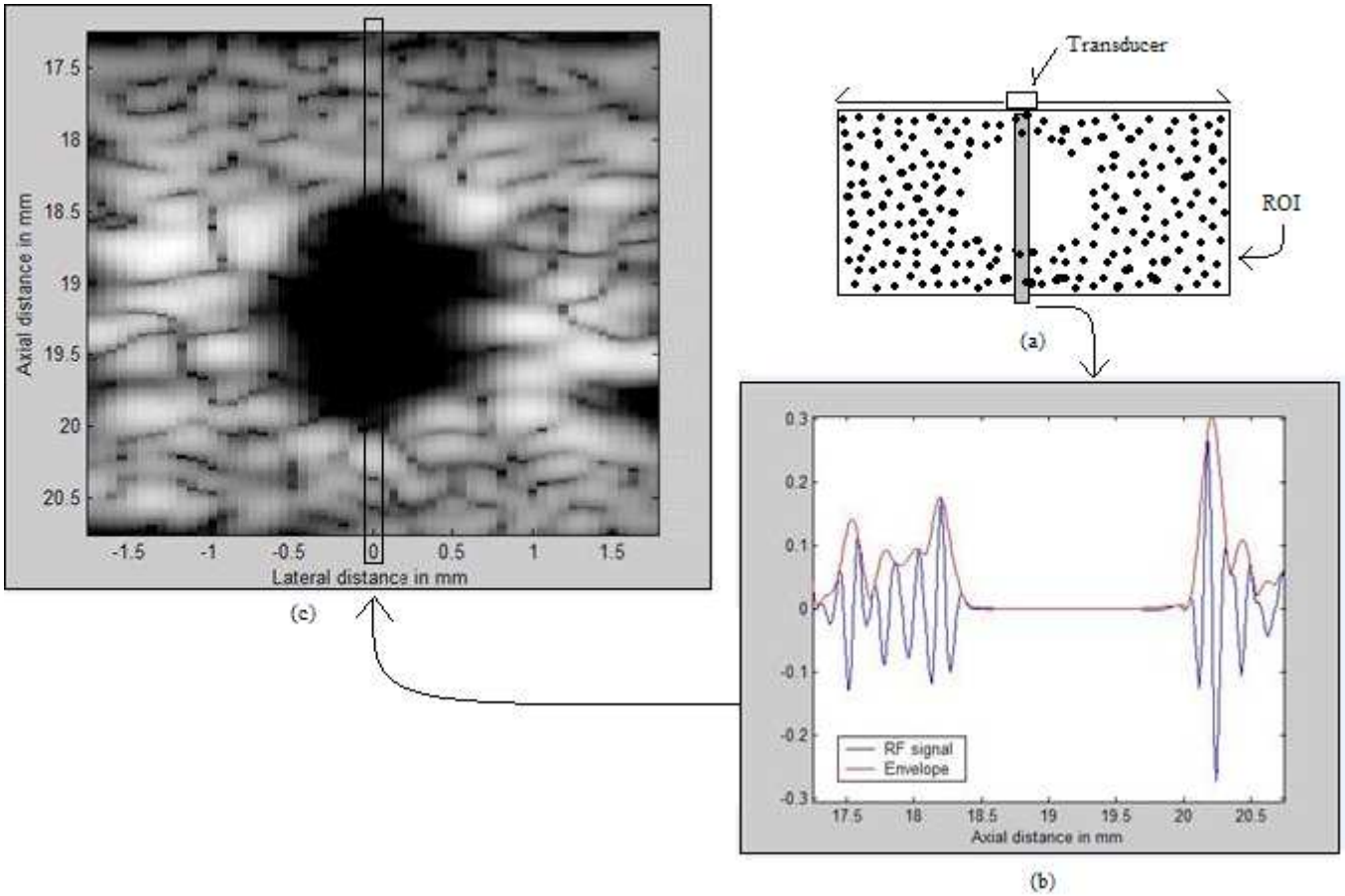

Figure 2.1: B-mode imaging configuration

1. The axial resolution is the spatial resolution in the direction of propagation of the wave and is restricted by the time duration of the signal emitted by the transducer (or equivalently, on its bandwidth). The two-point axial resolution of a system can roughly be approximated, assuming uniform frequency content in the bandwidth, as

$$\Delta x = \frac{c}{2B_0} \tag{2.1}$$

where:

c = speed of sound

B_0 = bandwidth of the signal

2. The lateral resolution is the spatial resolution on the axis perpendicular to the direction of propagation of the wave. While the axial resolution depends exclusively on the bandwidth of the emitted signal, the lateral resolution depends on the characteristics of the ultrasonic system. For a given geometry of a source, the beamwidth is a function of the position. The two-point lateral resolution is defined as

$$\Delta y = 2r \tan \varphi \tag{2.2}$$

where

r = depth of the target on the X axis

φ = half-beamwidth angle

2.1.2 Characteristics of common geometries for ultrasonic transducers

Two common types of transducers will be briefly discussed: nonfocused circular pistons and focused transducers.

Nonfocused transducers. The most representative geometry is the circular piston, which consists of a planar, circular surface with a uniform surface velocity [12]. For this geometry, the half-beamwidth angle between nulls is given by

$$\varphi = \arcsin \frac{3.83}{ka} \tag{2.3}$$

where

k = wave number of the acoustic wave

a = radius of the transducer

For Eq. (2.3) to be valid, the target must be in the far field of the transducer, i.e., the distance from the transducer to the target should be larger than the Rayleigh distance, which can be approximated by

$$R_{Rayleigh} = \frac{\pi a^2}{4\lambda} \tag{2.4}$$

where

λ = wavelength of the acoustic wave

a = radius of the transducer

It can be seen from Eq. (2.3) that the beamwidth for a planar piston has an inverse dependency on the radius of the transducer, which means that a larger transducer is more directive (has a narrower beamwidth) than a smaller one.

Focused transducer. The ultrasonic beam can be focused on a certain region (named focal region) to obtain high acoustic intensity and good lateral resolution. This can be accomplished by using a concave, spherically shaped transducer [10] which will produce a beam pattern that is focused close to its radius of curvature (ROC). This geometry is depicted in Figure 2.2.

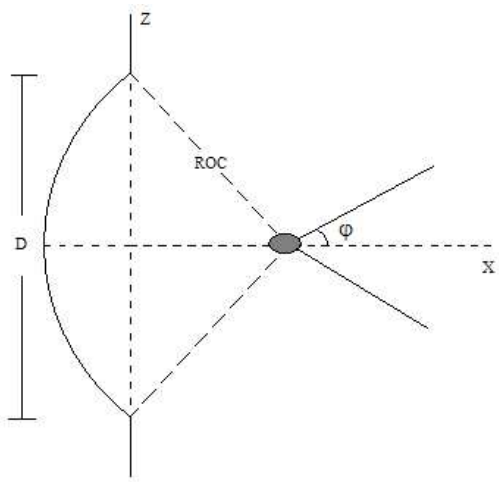

Figure 2.2: Geometry of a focused transducer

A parameter commonly used to describe a spherical transducer is the focal number or $f_{\#}$, which is defined as the ratio of the ROC and the diameter of the transducer:

$$f_{\#} = \frac{ROC}{D} \tag{2.5}$$

The lower the $f_{\#}$, the more focused the transducer is. The degree of focusing will have a direct impact on all the parameters of the diffraction pattern of the transducer.

The half-beamwidth spreading angle for depths beyond the focal region can be approximated as

$$\varphi = \arctan \frac{1}{2f_{\#}} \tag{2.6}$$

Another parameter defined for a focused transducer is the depth of focus, which is the -6 dB beamwidth in the direction of propagation, and is given by

$$F_z = 7.08\lambda f_{\#}^2 \tag{2.7}$$

Also, for a focused transducer, the -6 dB beamwidth on the cross-range axis at the ROC gives the lateral resolution at the focus:

$$F_D = 1.028\lambda f_{\#} \tag{2.8}$$

A transducer with a smaller value for $f_{\#}$ will have better lateral resolution at the focus according to Eq. (2.8), a shorter depth of focus according to Eq. (2.7), and a larger spreading angle according to Eq. (2.6). Hence, there is a trade-off involving the size of the ROI and the best lateral resolution.

In speckle-based images, several scatterers are present within a resolution cell. Because of this, the images have a granular appearance with bright and dark spots. The size of the speckle spot is known as correlation cell size [18]. The correlation cell size is in the same order of the size of the focal region [10], [18]. Approximate expressions (taken from [18] with the bandwidth B_0 given by the standard deviation of the pulse envelope shape) for the lateral and axial correlation cell sizes $S_{lateral}$ and S_{axial} are

$$S_{lateral} = 0.87\lambda f_{\#} \tag{2.9}$$

$$S_{axial} = \frac{0.91}{B_0} \tag{2.10}$$

2.2 Stripmap Synthetic Aperture

When a source with a larger physical aperture (diameter) is used, the beam is more directional and a better lateral resolution is achieved. That is the principle behind synthetic aperture, which encompasses a group of techniques to simulate a larger aperture using elements with a small physical aperture. The axial and lateral resolution will depend on the configuration used to synthesize the aperture.

The simplest SAFT configuration is called stripmap [37]. A simple diagram for a stripmap synthetic aperture system is depicted in Figure 2.3:

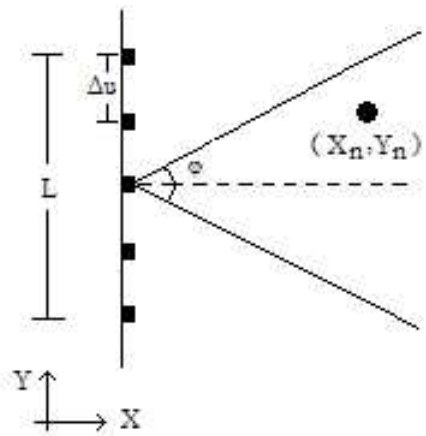

Figure 2.3: Configuration for stripmap imaging

On this configuration, the echoes are collected at evenly spaced positions with a distance of Δu across a distance L. The echoes from the reflector collected at the position $u = i\Delta u$, $i = 0, 1, 2...$ due to an ideal point target, assuming that the transducer transmits an spherical wave over a certain beamwidth given by θ, will occur at the time given by

$$\Delta t_u = \frac{2\sqrt{x_n^2 + (y_n - u)^2}}{c} \tag{2.11}$$

where

c = speed of sound

x_n = depth of nth target

y_n = azimuthal position of the nth target

The time delays are calculated assuming constant speed of sound. The factor of 2 comes from the fact that the time corresponds to a round trip between the transducer and the target.

2.2.1 SAFT signal processing for stripmap configuration

The reconstruction process can be performed using operations in the time domain with an algorithm known as backprojection [37], [38]. To find an approximate value of the reflectivity at a position (x, y), the backprojection algorithm adds coherently the data at the times given by Eq. (2.11) for every scanning position u.

Equation (2.11) maps the position (x, y) to a value of time corresponding to the start of an echo, but because the peak of the echo occurs at a later moment in time, the signals have to be deconvolved in order to apply the backprojection algorithm. If the deconvolution is not performed, the quality of the image will be degraded. For this purpose, the signal is correlated with a reference signal, which corresponds to a typical waveform emitted by the transducer (for a focused transducer, the signal can be the wave at the focus). The correlation is a measure of the similarity of two signals. If the received signal contains echoes (delayed versions of the emitted pulse), then the maximum of the correlation will occur at the positions in which such echoes start. The correlation can be expressed in terms of a convolution so this process is commonly referred as matched filtering, and the reference signal $s_R(t)$ as the matched filter:

$$s_M(t, u) = s(t, u) * s_R^*(-t) \tag{2.12}$$

where

$s_M(t, u)$ = matched filter signal

$s(t, u)$ = signal received at the scanning position u

In the radar community, the transmitted signal is a chirp (frequency modulated) pulse, which has a very large bandwidth and is highly asymmetric. Hence, the matched filtering process enhances the axial resolution. However,ultrasonic pulses are very limited in terms of bandwidth, so the matched filtering process degrades the axial resolution.

Data smearing across several points in the image occurs because of the finite physical aperture size. Beamforming improves the quality of the image because it exploits the redundancy of the measurements. Beamforming in the time domain is

accomplished using the backprojection algorithm, which consists on performing a weighted integral of the values of the received signal that correspond to time values that lie in the geometric place of the dispersion of a target point located at coordinates (x, y), which according to Eq.(2.11) is a hyperbola. The backproyected signal can be expressed as

$$s(x,y) = \int_{y-BW_x}^{y+BW_x} \alpha_u s_M \left(\frac{2\sqrt{x^2 + (y-u)^2}}{c}, u \right) du \tag{2.13}$$

where

BW_x = beamwidth of the signal at the depth x

α_u = apodization factor

s_M = matched filtered signal

When Eq. (2.13) is used, the backprojection operation will give higher values if it is applied at positions in which a target exists; however, the values that will be generated for positions in which no targets are present are not going to be equal to zero. This is the mechanism of sidelobe formation in SAFT. The apodization factor α_u is used to reduce the level of the sidelobes, at the expense of degrading the lateral resolution [13]. Only scanning positions that are inside the subaperture (i.e., the region of space that lies within the beamwidth of the transducer at a certain depth) are included in the integral.

The integral in practice will be replaced by a sum, and the values of x and y will be discretized to the values of the grid for which the image will be reconstructed. Because we are dealing with discrete-time signals, the value of the matched filtered signal is only known for discrete values of time; thus, interpolation should be used. However, if the sampling frequency is high enough, good performance is achieved without the need of interpolation.

It is also worth mentioning that SAFT reconstruction can be performed in the frequency domain using algorithms such as frequency interpolation [39] and range stacking [38]. These techniques are reported to have lower computational cost than their time domain counterparts.

2.2.2 Spatial resolution of stripmap synthetic aperture techniques

The improvement of the lateral resolution when using stripmap SAFT is mainly limited by the beamwidth of the transducer. Although in B-mode imaging a small beamwidth is desirable, in synthetic aperture imaging a larger beamwidth will cause more lines to be included in the subaperture for every depth and hence the uncertainty region can be further reduced. There is a relationship between the geometry of the transducer and the beamwidth, so the lateral resolution will also be dependent on the type of transducer used. For a circular piston of radius a, the limit on the lateral resolution is given by

$$\Delta y = \frac{a}{2} \tag{2.14}$$

In the case of a focused transducer, it has been shown in [40] that the geometric focus can be treated like a virtual source of ultrasound; therefore, the synthetic aperture processing can be accomplished by delaying the signals with respect to the position of the focus (and not the surface of the transducer, as in the case of a planar piston). The expression for the lateral resolution was shown to be

$$\Delta y = 0.82 f_{\#} \lambda \tag{2.15}$$

It can be noted that in both cases, the lateral resolution is only dependent on the geometry of the transducer and no longer depends on the depth of the ROI. Also, for a focused transducer, the theoretical lateral resolution for SAFT is even less than the best achievable for B-mode, which is given by Eq. (2.8). However, due to the presence of sidelobes generated during the signal processing, the contrast resolution of the images generated using SAFT is worse than that achievable with a B-mode image when the ROI is at the physical focus of the transducer.

The concepts developed in this chapter will be illustrated though a simulation corresponding to a ROI containing a single point scatterer. The simulated transducer is spherical with $f_{\#}$ of 1, 50% bandwidth and a center frequency of 6 MHz. The speed of sound was set equal to 1500 m/s, which yields a wavelength λ equal to 250 μm. The results for the simulations are shown in Figure 2.4. Figure 2.4(a) shows the B-mode image generated when the scatterer is at the focus of the transducer, with a lateral resolution of 275 μm which is very close to the expected value given by Eq. (2.8). Figure 2.4(b) corresponds to the case when the scatterer is 3 mm beyond the focus of the transducer. The beam spreading is clearly noticeable and the lateral resolution,

which has a value of 1575 μm, is severely degraded. Figure 2.4(c) shows the result of applying SAFT processing to the out of focus B-mode image. Hamming apodization was used for the reconstruction. The lateral resolution is equal to the one achieved when the scatterer was at the focus of the transducer (275 μm). However, it can be seen that sidelobes were formed during the reconstruction. Figure 2.4(d) shows the beam profiles (in decibels) at the depths of maximum mainlobe (blue curve) and sidelobe (red curve) intensities. The maximum intensity of the sidelobes is 26 dB below the maximum intensity of the mainlobe.

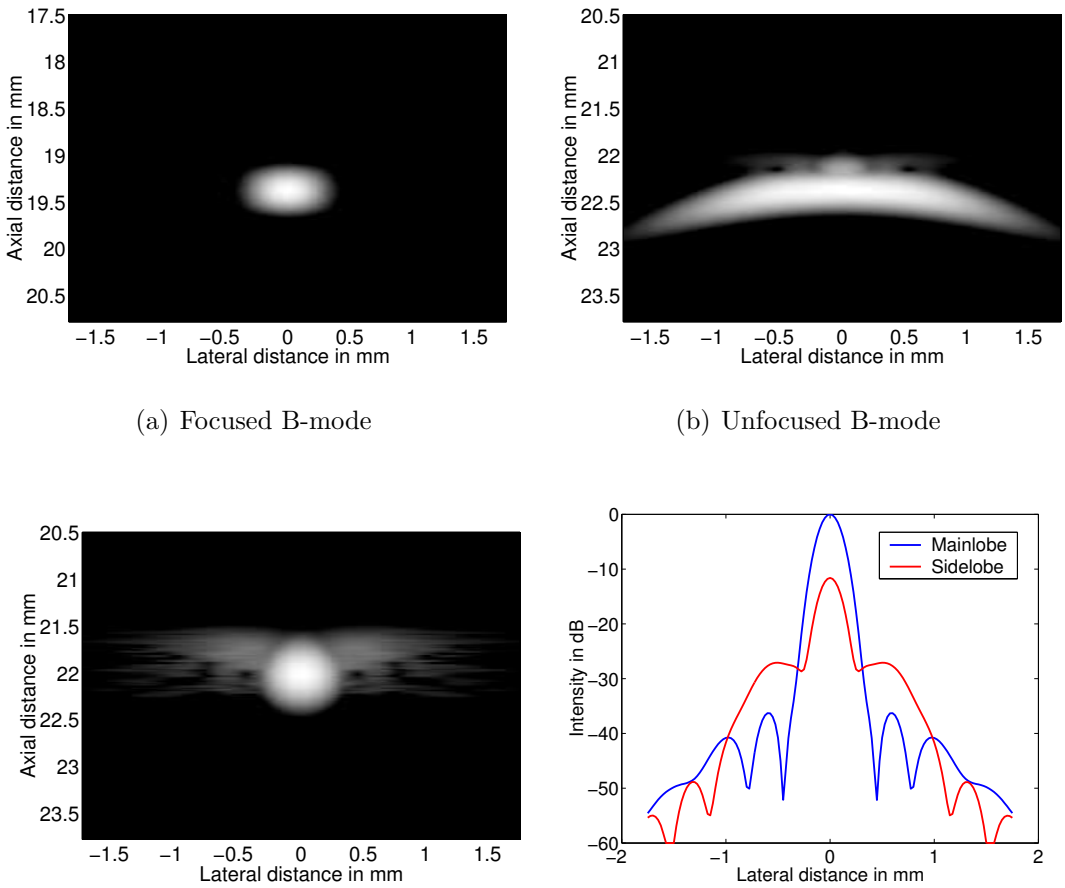

(a) Focused B-mode

(b) Unfocused B-mode

(c) SAFT

(d) Intensity profiles

Figure 2.4: Reconstructed images using conventional techniques for a single point scatterer

This concludes the brief overview of monostatic conventional imaging techniques. The procedures for image generation using B-mode and SAFT have been outlined. The spatial resolution for targets on focus and out of focus have been analyzed through governing equations and a simple example. Also, it has been shown that SAFT improves the lateral resolution at the cost of sidelobe generation. In the next chapter, the formulation of monostatic pulse-echo imaging using regularization will be described.

CHAPTER 3

REGULARIZATION THEORY FOR IMAGE RECONSTRUCTION

3.1 Pulse-Echo Imaging Problem Using an Inverse Problems Formulation

Consider the configuration shown in Figure 3.1.

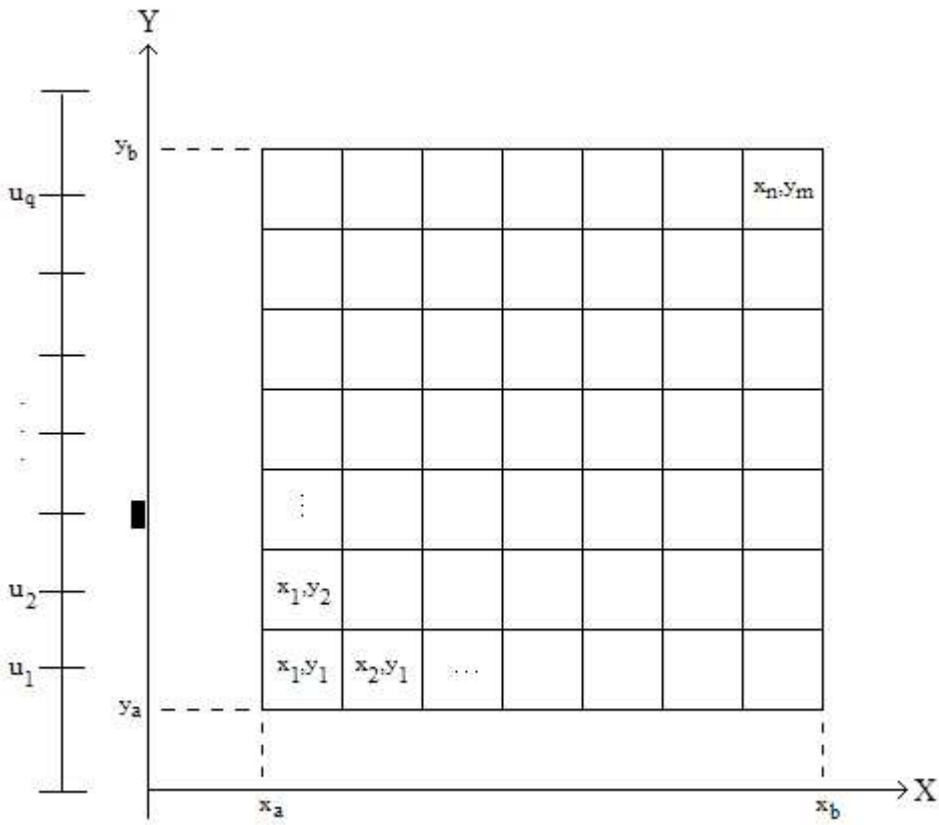

Figure 3.1: Configuration for pulse-echo imaging inversion

The ROI is a square region with $x_a \leq x \leq x_b$ and $y_a \leq y \leq y_b$. The transducer

is moved across the Y axis, and the pulse-echo data is acquired at locations u_l, $1 \leq l \leq q$. The received signal is sampled at discrete times t_k, $1 \leq k \leq p$; the time signal recorded at the position u_l will be denoted by $g(t, u_l)$.

The ROI is also discretized, with the discrete values of x and y denoted by x_i, $1 \leq i \leq n$ and y_j, $1 \leq j \leq m$. The reflectance of the ROI will be assumed to be constant for each pixel and will be denoted by $r_{(x_i,y_j)}$.

The spatially variant impulse response of the transducer (i.e., the signal that would be received if a point target of unitary amplitude is at the coordinates $(\hat{x}, \hat{y})$ relative to the transducer) will be denoted by $s_{\hat{x},\hat{y}}(t)$. Such function depends on the geometry and time impulse response of the transducer, and is in general a complicated function for which no suitable closed form exists. However, for simulations it can be computed using numerical methods like the FIELD II [41] program; or for experiments it can be measured using a hydrophone or the wire technique [42]. The spatial impulse response has to be calculated for the acquisition time interval of the pulse-echo data and sampled at the same sample frequency used in the acquisition process.

If the transducer is placed at the location u_l, the received pulse-echo data will be the sum of the contribution of the time impulse response of all the pixels of the ROI scaled by the values of the reflectances of each pixel, so that $g(t, u_l)$ can be expressed as

$$g(t, u_l) = \sum_{i=1}^{n} \sum_{j=1}^{m} r(x_i, y_j) s_{x_i, y_j - u_l}(t) \tag{3.1}$$

For the last equation, the fact that the relative coordinates of the point (x_i, y_j) when the transducer is at the point $(0, u_l)$ are equal to $(x_i, y_j - u_l)$ has been used. Since the signals $g(t, u_l)$ and $s_{\hat{x},\hat{y}}(t)$ are known for discrete values of time, the last equation can be expressed as:

$$g(t_k, u_l) = \sum_{i=1}^{n} \sum_{j=1}^{m} r(x_i, y_j) s_{x_i, y_j - u_l}(t_k) \tag{3.2}$$

Both sequences $g(t_k, u_l)$ and r_{x_i,y_j} are two-dimensional, so that in order to express Eq. (3.2) as a linear system, the vectors corresponding to $g(t_k, u_l)$ and r_{x_i,y_j}have to be stacked to form a one-dimensional sequence. With this modification, Eq. (3.2) can be rewritten in matrix form as

$$A_{PE}\begin{bmatrix}\begin{bmatrix} r_{x_1,y_1} \\ r_{x_2,y_1} \\ \vdots \\ r_{x_n,y_1} \end{bmatrix} \\ \begin{bmatrix} r_{x_1,y_2} \\ r_{x_2,y_2} \\ \vdots \\ r_{x_n,y_2} \end{bmatrix} \\ \vdots \\ \begin{bmatrix} r_{x_1,y_m} \\ r_{x_2,y_m} \\ \vdots \\ r_{x_n,y_m} \end{bmatrix}\end{bmatrix} = \begin{bmatrix}\begin{bmatrix} g_{t_1,u_1} \\ g_{t_2,u_1} \\ \vdots \\ g_{t_p,u_1} \end{bmatrix} \\ \begin{bmatrix} g_{t_1,u_2} \\ g_{t_2,u_2} \\ \vdots \\ g_{t_p,u_2} \end{bmatrix} \\ \vdots \\ \begin{bmatrix} g_{t_1,u_q} \\ g_{t_2,u_q} \\ \vdots \\ g_{t_p,u_q} \end{bmatrix}\end{bmatrix} \tag{3.3}$$

where

$$A_{PE} = \begin{bmatrix} \begin{bmatrix} s_{x_1,y_1-u_1}(t_1) \\ s_{x_1,y_1-u_1}(t_2) \\ \vdots \\ s_{x_1,y_1-u_1}(t_p) \end{bmatrix} & \begin{bmatrix} s_{x_2,y_1-u_1}(t_1) \\ s_{x_2,y_1-u_1}(t_2) \\ \vdots \\ s_{x_2,y_1-u_1}(t_p) \end{bmatrix} & \cdots & \begin{bmatrix} s_{x_n,y_m-u_1}(t_1) \\ s_{x_n,y_m-u_1}(t_2) \\ \vdots \\ s_{x_n,y_m-u_1}(t_p) \end{bmatrix} \\ \begin{bmatrix} s_{x_1,y_1-u_2}(t_1) \\ s_{x_1,y_1-u_2}(t_2) \\ \vdots \\ s_{x_1,y_1-u_2}(t_p) \end{bmatrix} & \begin{bmatrix} s_{x_2,y_1-u_2}(t_1) \\ s_{x_2,y_1-u_2}(t_2) \\ \vdots \\ s_{x_2,y_1-u_2}(t_p) \end{bmatrix} & \cdots & \begin{bmatrix} s_{x_n,y_m-u_2}(t_1) \\ s_{x_n,y_m-u_2}(t_2) \\ \vdots \\ s_{x_n,y_m-u_2}(t_p) \end{bmatrix} \\ \vdots & \vdots & & \vdots \\ \begin{bmatrix} s_{x_1,y_1-u_q}(t_1) \\ s_{x_1,y_1-u_q}(t_2) \\ \vdots \\ s_{x_1,y_1-u_q}(t_p) \end{bmatrix} & \begin{bmatrix} s_{x_2,y_1-u_q}(t_m) \\ s_{x_2,y_1-u_q}(t_2) \\ \vdots \\ s_{x_2,y_1-u_q}(t_p) \end{bmatrix} & \cdots & \begin{bmatrix} s_{x_n,y_m-u_q}(t_1) \\ s_{x_n,y_m-u_q}(t_2) \\ \vdots \\ s_{x_n,y_m-u_q}(t_p) \end{bmatrix} \end{bmatrix}$$

In this formulation, the matrix A_{PE} represents the numerical synthesis of the Green's function of the system. If the system of equations shown in Eq. (3.3) can be solved, then the reflectances of the ROI can be recovered based on the measured data. The rest of this chapter will show this can be achieved by using regularization methods and discuss the implementation of the techniques that have been used on the simulations performed for this study.

3.2 Least Squares and Generalized Solution

Consider the following set of equations:

$$Ax = y \tag{3.4}$$

The three possible scenarios are as follows:

1. The system is full rank; i.e., the number of equations equals the number of unknowns. In this case there is only one solution which is given by

$$\hat{x} = A^{-1}y \tag{3.5}$$

2. The equation matrix A has more columns than rows; i.e., there are more equations than unknowns. An exact solution for the system does not exist, so this problem is solved in the mean square sense. The solution is chosen to be the vector x that satisfies the least squares equation

$$\hat{x} = \arg\min_{x} ||y - Ax||_2^2 \tag{3.6}$$

3. The equation matrix A has more rows than columns; i.e., there are more unknowns than equations. There are infinite many solutions for this type of system, which is also solved in a mean square sense. The solution $\hat{x}$ is chosen to be the minimum energy solution to the least squares equation, which is also the solution to cases (1) and (2) and is given by

$$\hat{x} = \arg\min_{x} ||x||_2^2 \text{ subject to } \min ||y - Ax||_2^2 \tag{3.7}$$

An important tool for the solution of linear systems is the *pseudoinverse*. For a matrix A, its pseudoinverse is denoted by A^+. Using singular value decomposition, we can express:

$$A = USV^T \tag{3.8}$$

with U and V unitary matrices and S a diagonal matrix with the eigenvalues of A in decreasing order over the main diagonal. The matrix S^+ is constructed by transposing S and replacing the non-zero entries by their reciprocals. The pseudoinverse $A+$ is then defined as

$$A^+ = VS^+U^T \tag{3.9}$$

The pseudoinverse of a full rank matrix is equal to its inverse, that is, $A^+ = A^-1$. It can be shown [43] that the solution to Eq. (3.7) can be expressed in terms of the pseudoinverse of the forward operator as

$$\hat{x} = A^+y \tag{3.10}$$

3.3 Regularization

The problem with the pseudoinverse solution arises from the fact that the system defined by Eq.(3.4) can be unstable. The stability of a linear system is dependent on the linear independence among its equations. The condition number of a matrix is the ratio between its largest and the smallest singular value, and gives a measurement of the stability of the system. To see why, we can rewrite Eq. (3.10) first without noise in the data:

$$\hat{x} = A^+y = \sum_{i=1}^{r} \frac{u_i^T y}{\sigma_i} \tag{3.11}$$

The terms $u_i^T y$ are known as the *generalized Fourier coefficients*; a system is said to satisfy the discrete Picard condition if the terms $u_i^T y$ on the average decay faster than the corresponding eigenvalues σ_i [44].

Now for the case where the ideal data y is contaminated with noise labeled as w, we can write

$$\hat{x} = A^+(y + w) = A^+y + A^+w \tag{3.12}$$

and using the SVD decomposition

$$\hat{x} = \sum_{i=1}^{r} \frac{u_i^T y}{\sigma_i} + \sum_{i=1}^{r} \frac{u_i^T w}{\sigma_i} \tag{3.13}$$

Even though the eigenvalues of the matrix A decrease, the terms $u_i^T y$ decrease accordingly so that the contributions of y are bounded; however, the terms $u_i^T w$ do not satisfy the discrete Picard condition so that the noise is amplified and the solution is distorted. Since the amplification of the noise depends on the reciprocal of the eigenvalues, a large condition number means that the matrix is more unstable.

To counteract the noise amplification, the formulation of the inverse problem has to be modified so that it becomes stable even in the presence of noise by incorporating *a priori* information about the relevant features of the desired image. This approach is known as *regularization*.

A regularization method is defined as an inversion method dependent on a parameter α (called the regularization parameter) which yields a family of approximate solutions. In a noiseless case, the best solution will be obtained if $\alpha = 0$, i.e., if no regularization is applied. In the presence of noise, however, the value of α should be selected so that the modified system is stable at the cost of loosing features of the data to be recovered. Hence, one must select a value of α that not only ensures that the system will be stable for the expected values of signal-to-noise ratio (SNR) but also preserves most of the features of the data to be reconstructed, so that the choice of an appropriate value of α becomes extremely important.

3.4 TSVD Regularization

The most intuitive way to compensate for a high condition number in a linear problem is to limit the lower value of the eigenvalues so that that the ratio $\sigma_{max}/\sigma_{min}$ is constrained to a certain value. This regularization is called truncated singular value decomposition (TSVD)[44] and can be expressed as

$$\hat{x} = \sum_{i=1}^{r} \frac{w_\alpha(\sigma_i) u_i^T y}{\sigma_i} \tag{3.14}$$

where

$$w_\alpha(\sigma_i) = \begin{cases} 1, & \text{if } \sigma_i \leq \alpha \\ 0, & \text{else} \end{cases}$$

For this method, the regularization parameter is the lower bound for the eigenvalues. Even though this solution is very straightforward, the singular value decompo-

sition of the matrix A, which is computationally demanding for large scale systems, has to be performed in order to apply this technique.

3.5 Tikhonov Regularization

One of the most common regularization methods is the *Tikhonov regularization* [45], which consists in modifying the least squares equation by adding an additional cost function equal to the square l_2 norm of a linear transformation of x:

$$\hat{x} = \arg\min_x \left\{ ||y - Ax||_2^2 + \alpha^2 ||Lx||_2^2 \right\} \tag{3.15}$$

The advantage of Tikhonov regularization is that since the modified cost function is quadratic, the gradient of Eq. (3.15) is linear, and the solution in the mean square sense is given by the following linear system:

$$(A^T A + \alpha^2 L^T L)\hat{x}_{tik} = A^T y \tag{3.16}$$

The particular choice of the linear transformation matrix L will determine the features that this regularization method will enhance. Two common choices are the following:

1. The identity matrix I, for which the cost function is simply the energy of the image. The inclusion of this term implies a penalization of solutions with large norm, so it favors low energy solution. Using the SVD of the system, it can be shown that the solution can be expressed as

$$\hat{x} = \sum_{i=1}^{r} \frac{w_\alpha(\sigma_i) u_i^T y}{\sigma_i} \tag{3.17}$$

where

$$w_\alpha(\sigma_i) = \frac{\sigma_i^2}{\sigma_i^2 + \alpha^2}$$

The effect is a filtering of the smaller singular values, smoother than the case of the TSVD regularization, with the advantage that the SVD of the system does not need to be calculated. Notice that for large α so that $AA^T < \alpha^2 I$, the asymptotic solution for $\hat{x}$ is given by

$$\hat{x}_{\alpha\to\infty} = \frac{A^T y}{\alpha^2} \tag{3.18}$$

This last equation basically shows that the solution for large α will correspond to the adjoint operator A^T applied to the data and scaled by a factor of $\frac{1}{\alpha^2}$. A direct consequence is that asymptotically with α, the estimate $\hat{x}$ will go to zero.

2. The discrete approximation to the gradient,

$$L = \begin{bmatrix} 1 & -1 & 0 & 0 & \cdots & 0 \\ 0 & 1 & -1 & 0 & \cdots & 0 \\ 0 & 0 & 1 & -1 & \cdots & 0 \\ \vdots & \ddots & \ddots & \ddots & \ddots & \vdots \\ 0 & 0 & 0 & \cdots & 1 & -1 \end{bmatrix} \tag{3.19}$$

This term favors solutions that are locally smooth, so it favors reconstructions of images that consist of several regions because it preserves the edges better than in the case of the identity matrix and also enforces smoothness away from the edges.

3.6 Generalized Tikhonov Regularization

Tikhonov regularization consists in adding a quadratic cost function to the least squares equation. Even though a quadratic cost function yields to a linear problem, such penalization may not be optimum for a given problem. A generic approach known as *generalized Tikhonov regularization* [46] is given by

$$\hat{x} = \arg\min_x \left\{ ||y - Ax||_2^2 + \alpha^2 f(x) \right\} \tag{3.20}$$

The term $f(x)$ is known as penalty or regularization cost function. The term $||y - Ax||_2^2$ is referred to as the data discrepancy or fit-to-data function. Several choices of nonquadratic cost function have been studied and the simplest one is the l_k^k norm with $k \neq 2$. The l_k^k norm of a vector x, denoted as $||x||_k^k$, is defined as

$$||x||_k^k \triangleq \sum_{i=1}^{n} |x|_i^k \tag{3.21}$$

Figure 3.2 shows a comparison among three different norms. It can be seen that as the value of k decreases, the penalization is less severe for larger values and more severe for smaller values of the argument of the l_k^k norm function. Because of this, the

features in the image are better preserved than in the case of quadratic regularization, and small components of the image which correspond to noise can be better filtered while the large values which correspond to the features of the desired image can be better preserved. A well-studied case corresponds to the l_1^1 norm used with the matrix L equal to the discrete gradient approximation, and is known as the *total variation regularization* [47]. This regularization method was developed for edge-preserving regularization, and works better than the equivalent quadratic Tikhonov method.

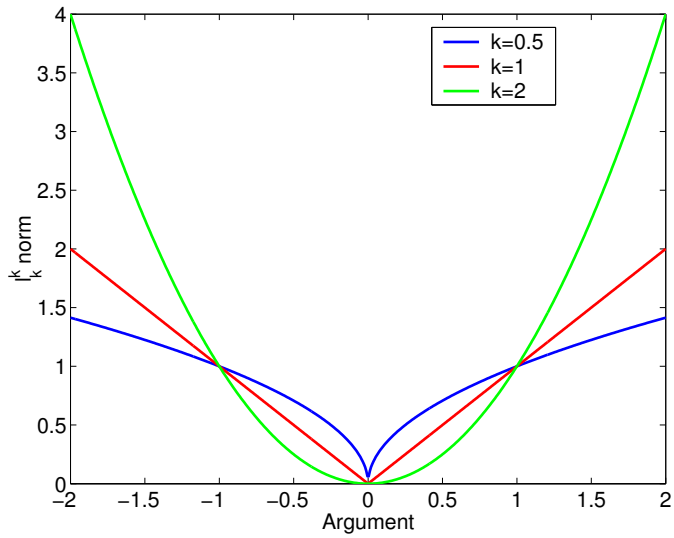

Figure 3.2: Comparison of the l_k norm with different values of k

A nonquadratic l_k^k norm regularization cost analogous to the quadratic Tikhonov regularization can be expressed as

$$\hat{x} = \arg\min_x \left\{ ||y - Ax||_2^2 + \alpha^2 ||Lx||_k^k \right\} \tag{3.22}$$

One difficulty of this particular choice of cost function is that the l_k^k norm for values of k less or equal than 1 is not differentiable at zero. Because of this, the cost function can be rewritten as

$$\hat{x} = \arg\min_x \left\{ ||y - Ax||_2^2 + \alpha^2 \sum_{i=1}^{N} \left(|(Lx)_i|^2 + \beta \right)^{k/2} \right\} \tag{3.23}$$

where β is a small, positive constant. The gradient of the last equation with respect of x can be calculated, resulting in the following equation:

$$\left(A^T A + \alpha^2 L^T W_\beta(x) L\right) x = A^T y \tag{3.24}$$

where

$$W_\beta(x) = \frac{k}{2} \operatorname{diag}\left(\left(|(Lx)_i|^2 + \beta\right)^{1-k/2}\right) \tag{3.25}$$

This nonlinear equation can be solved iteratively. Starting with an initial guess $x^{(0)}$ and using the fact that at convergence $x^{(n+1)} = x^{(n)}$,

$$\left(A^T A + \alpha^2 L^T W_\beta(x^{(n)}) L\right) x^{(n+1)} = \gamma A^T y + (1-\gamma) H(x^n) x^{(n)} \tag{3.26}$$

where $\gamma \leq 1$ is a parameter controlling the relative amplitude of the terms in the modified Hessian update equation. The iterative process is stopped when the difference in the norm between successive iterations is small enough, that is, until $||x^{(n+1)} - x^{(n)}||_2^2 / ||x^{(n+1)}||_2^2 < \delta$, where δ is the desired tolerance.

It should be noted also that this particular regularization method has three regularization parameters. The parameter α is the one that controls the amount of regularization imposed. The inclusion of additional regularization parameters adds more degrees of freedom to find a more accurate solution, but at the same time complicates the parameter selection process.

3.7 Automatic Regularization Parameter Selection Techniques

The choice of appropriate values for the regularization parameter is crucial to obtain good results. Even though for simulations one can estimate a range of optimal parameters by using visual inspection with a set of reference images, in practice the desired images are not available, so quantitative parameter selection methods need to be used. Several parameter selection techniques are available and have been explored in the specialized literature:

1. The discrepancy principle [45] was originally introduced by Morozov [48]. The least squares solution to a linear problem involves the minimization of the residual $||y - Ax||_2^2$. For simplicity, it will be assumed that there exists a unique solution denoted by $\hat{x}$ for which the residual is equal to zero for noiseless measurements y, that is, $||y - A\hat{x}||_2^2 = 0$. However, in the presence of additive noise denoted by w, the residual when $x = \hat{x}$ is equal to $||w||_2^2$. For the noisy

case, the value of x that minimizes the residual will be in general different than $\hat{x}$. The discripancy principle states that the regularization parameter α should be chosen to be the largest of the set that generates a solution that yields a residual equal to a certain constant, that is

$$\alpha_{OPT} = \text{ max } \alpha \text{ subject to } ||y - A\hat{x}_\alpha||_2^2 = k\delta \tag{3.27}$$

where δ is the expected value of the minimum residual and k is a constant such that $k \geq 1$. For stochastic settings, this is equivalent to knowing the statistics (mean and variance) of the random additive noise. The main drawback of this method is that the value of the desired residual is usually unknown or only roughly estimated in real problems.

2. The L-curve method was first introduced by Lawson and Hanson [49] and popularized by Hansen [50]. It consists in plotting the norm of the regularization cost ($||L\hat{x}(\alpha)||_2$ for the case of Tikhonov) versus the norm of the residual ($||y - A\hat{x}(\alpha)||_2$) in a log-log scale. As in the case of the discrepancy principle, when there is noise present in the measurements, the residual is expected to be the energy of the noise and not identically zero. For small values of regularization parameters, the residual will be too small and because the solution will typically be driven by the noise, the regularization cost will be high. As the regularization parameter increases, the residual will increase, and the regularization cost will decrease. The rate of this change, however, is not uniform. Intuitively, one should select a point in which neither the regularization cost nor the residual dominate the behavior of the curve. If both the cost and the residual vary smoothly with α (which is the case for quadratic Tikhonov regularization), the curve that is formed typically has an L shape (hence the name of this method), and the optimal value of α is chosen to be the one that corresponds to the corner of this curve (typically chosen as the point of maximum curvature), as shown in Figure 3.3.

   The main limitation of this selection technique is that the L shape of the curve is not guaranteed for every regularization method; an important example is TSDV (see [46] for a complete analysis). The applicability of this method has been studied for l_k^k norm generalized Tikhonov regularization in [51]. For Tikhonov regularization, even though the curve will have a L shape, it will be

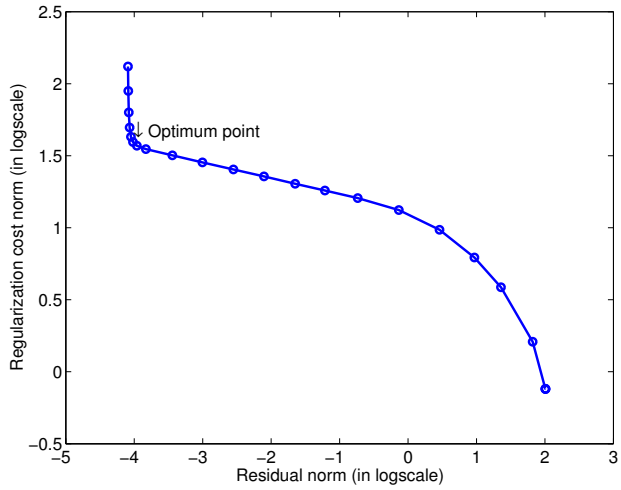

Figure 3.3: L-curve method

non convergent if the generalized Fourier coefficients of the forward operator do not satisfy the discrete Picard condition [52]. Also when the residual is very small, the L-curve fails to converge [53].

3. The generalized cross-validation method (GCV) was developed by Golub et al. [54]. It is based on the minimization of the predictive error and has a similar derivation to the one of the unbiased predictive risk estimator (UPRE) method [46]. Unlike UPRE, GCV does not require knowledge of the statistics of the noise. Because the ideal data is not available, an estimate of the error is derived from the measurements as follows: for a fixed regularization parameter α, one point of the measured data is removed from the measurements, and its value is estimated using the modified forward model and the rest of the measurements, with a corresponding estimation error. This procedure is repeated for all points in the measurements data set. The predictive error is defined as the average of the estimation errors for a fixed α. The optimum value of α is the one that minimizes the predictive error because it can discriminate better the data from the noise in the measurements. The GCV estimator for the predictive error can be calculated as

$$G(\alpha) = \frac{||y - A\hat{x}(\alpha)||_2^2}{[\text{trace}(I - A^T A^{\#}(\alpha) A)]^2} \tag{3.28}$$

where $A^{\#}$ is the linear operator relating y and $\hat{x}(\alpha)$, i.e., $\hat{x}(\alpha) = A^{\#}y$.

The optimum parameter is the one that yields the the minimum value of the GCV curve. An example of the appearance of a GCV curve is shown in Figure 3.4.This parameter selection technique does not suffer from the limitations that that the L-curve has. However, it has its own drawbacks: the GCV curve can have a very flat minimum, which makes it difficult to choose an appropriate parameter value. Also, GCV has been shown not to converge to the optimum parameter when the noise is correlated to the signal [50]. That is not the case for the L-curve, provided that the noise does not satisfy the Picard condition. Additionally, its calculation is computationally expensive compared to other parameter selection techniques.

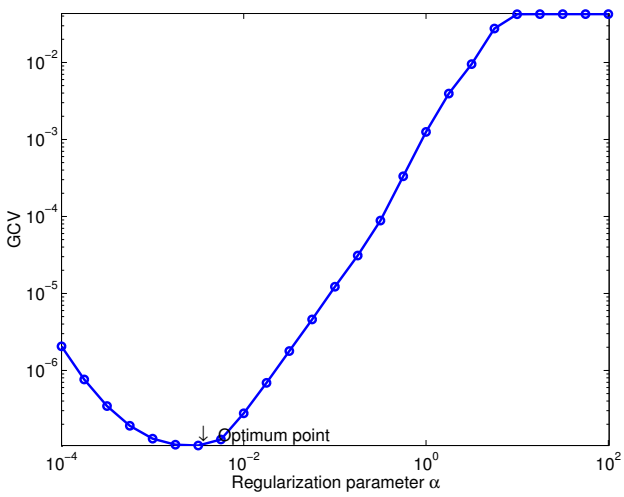

Figure 3.4: GCV method

This concludes the discussion of the inverse problems formulation for monostatic pulse-echo imaging. An overview of inverse problems theory was given, including the issue of noise amplification. Regularization was introduced as a method to stabilize the inverse problem and find meaningful solutions. Among the different techniques, l_k^k norm Tikhonov regularization and its implementation were described. Also, techniques for regularization parameter selection have been discussed. The next chapter will show through simulations the result of applying these techniques to pulse-echo imaging.

CHAPTER 4

SIMULATIONS

Several simulations were run in order to test the performance of the reconstruction using regularization approaches. The simulated data were generated using Field II and correspond to using focused transducers in a medium with speed of sound equal to 1500 m/s. The simulated transducers have a central frequency of 6 MHz (which corresponds to a wavelength of 250 μm) and a focal distance of 19 mm. The sampling frequency was set to 60 MHz. Other parameters such as the bandwidth, the focal number and the distance between the ROI and the focus were not held constant for all simulations.

The spectrum of the transmit-receive impulse response of the transducer, $P(f)$, was modeled as

$$P(f) = f \exp\left(-\frac{2.9(f - \kappa f_0)^2}{BW^2}\right) \tag{4.1}$$

where

f = frequency

f_0 = central frequency of the transducer

BW = -3 dB transmit-receive bandwidth of the transducer

The variable κ in Eq. (4.1) is used to properly adjust the -3dB frequency band of the transducer. For the present work, κ ranged between 0.9 and 1.

The transducer was apodized to smooth the variations of the acoustic field. The apodization function $A(r)$ was chosen to be a Hann function defined as

$$A(r) = \epsilon + (1 - \epsilon)\cos\left(\frac{\pi r}{D}\right) \tag{4.2}$$

where

r = distance to the center of the tranducer

D = diameter of the transducer

The variable ϵ in Eq. (4.2) is used to control the level of apodization for the surface of the transducer. For the present work, ϵ was set to be 0.1.

The ROIs used for the simulations consist on two-dimensional, square regions of 3 by 3 mm. The ROIs were divided into two concentric subregions with the inner one having a diameter of 1 mm.

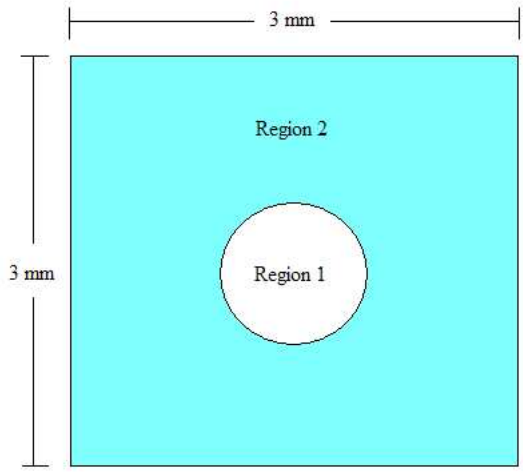

Figure 4.1: Schematic diagram of the region of interest for the simulations

The subregions will be from now on referred as Region 1 and Region 2, as shown on Figure 4.1. The ROIs were discretized using a grid of a quarter of a wavelength ($\frac{\lambda}{4}$) at the central frequency, resulting in images of 49 by 49 pixels. A total of 750 scatterers were distributed on the ROIs, resulting in a scatterer density of approximately 2.5 scatterers every eight pixels. Because the highest bandwidth and the smallest focal number used are 100% and 1, respectively, the smallest resolution cell used in the simulations corresponds roughly to $0.5\lambda^2$. This means that a minimum scatterer density of 2.5 scatterers per resolution cell is guaranteed for every simulation. This is above the limit of 2 scatterers per resolution cell determined in [55] by Tuthill et al. for sparse scatterer density in speckle based ROIs. The minimum value of 2.5 scatterers per resolution cell was also chosen to avoid using a large grid size which would increase the computation time of the algorithm.

Two ROIs were used for the simulations: the first with Region 1 containing scatterers of peak reflectivity amplitude 10 times higher than the ones in Region 2, and the second with Region 1 containing scatterers of peak reflectivity amplitude 10 times lower than the ones in Region 2. For both ROIs, the same spatial distribution of

the scatterers was used. The reflectivity amplitudes of the scatterers vary uniformly in an interval of 20% around the maximum amplitude value for each region. Both ROIs are shown in Figure 4.2.

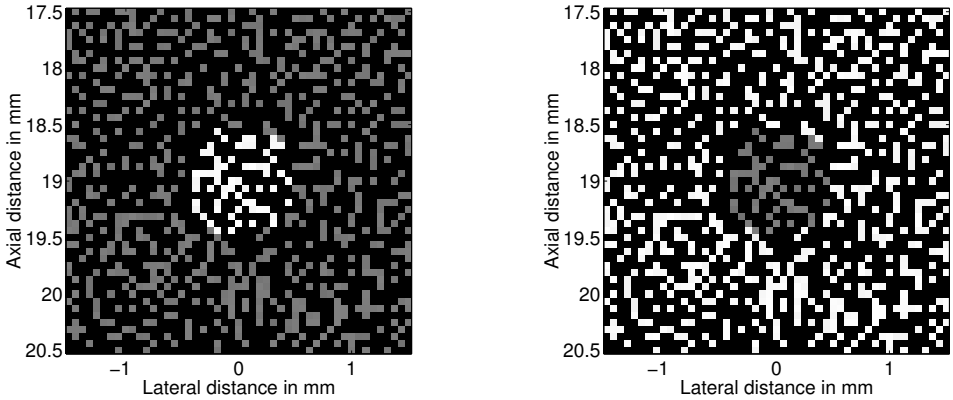

(a) First scatterer distribution

(b) Second scatterer distribution

Figure 4.2: ROIs used for the simulations

Zero-mean Gaussian noise was used to contaminate the data. The signal-to-noise ratio (SNR) for the present study is defined as

$$SNR = 10 \log \left(\frac{||g||_2^2}{||w||_2^2} \right) \tag{4.3}$$

where

g = pulse-echo data signal (without noise)

w = additive noise

The same realization of noise was scaled in order to change the SNR so that a fair comparison of the effect of several parameters can be performed.

The normalized mean square error (MSE) was used in order to numerically evaluate the performance of the reconstruction. The normalized MSE is defined here as the square of the l_2^2 norm of the reconstruction error normalized with respect to the square l_2^2 norm of the desired data:

$$MSE = \frac{||x - \hat{x}||_2^2}{||x||_2^2} \tag{4.4}$$

where

x = ideal reflectivity distribution

$\hat{x}$ = reconstructed data

As a complement, the reconstructed images using conventional imaging techniques (B-mode and SAFT imaging) together with the regularization reconstructions are also shown for selected values of SNR of 40, 30, and 20 dB. All the images are shown in a logarithmic scale with a dynamic range of 40 dB.

Several regularization techniques were introduced in Chapter 3. For the present work, generalized Tikhonov was selected as the regularization method. This method has several properties that makes it a reasonable choice:

1. It is a generic framework that allows to regularize an inverse problem in a very flexible way.

2. It is computationally easy to implement.

3. It allows the use of well studied automatic regularization parameter selection techniques such as GCV and the L-curve.

During the rest of this chapter, the effect of different parameters involved in the reconstruction process will be explored in order to understand the feasibility of regularization reconstruction applied to pulse-echo imaging. Two types of parameters will be explored:

1. Regularization parameters (discussed in Section 4.1). This includes all the parameters involved in solving the regularized inverse problem formulation of Eq. (3.23) for a fixed forward model matrix A.

2. Imaging system parameters. That is, the parameters that affect the forward model used for the image reconstruction. Depending on the stability of the forward model, the regularization procedure will be more or less effective. Three imaging system parameters were explored for the present work:

   - The relative pulse-echo bandwidth of the transducer (discussed in Section 4.2), defined as in [42] to be the ratio of the -3 dB transmit-receive bandwidth of the transducer and its central frequency.
   - The $f_{\#}$ of the transducer (discussed in Section 4.3), as defined in Eq. (2.5).
   - The distance between the region of interest (ROI) and the focal depth of the transducer (discussed in Section 4.4).

4.1 Choice of the Regularization Parameters

The appropriate choice of regularization parameters, as discussed in Chapter 3, is crucial in the performance of regularization reconstructions. As shown in Eq. (3.23), there are four parameters that have to be chosen for generalized Tikhonov regularization. In the present section, the criteria for the selection of each parameter will be discussed.

4.1.1 Choice of regularization matrix L

The regularization matrix L can be chosen as any stabilizing linear operator that includes *a priori* knowledge of the solution of the problem. In the case of speckle-based images, for which the reflectivity distribution has a random nature by definition, the optimum choice of L is not clear. The most natural way of regularizing an inverse problem is to remove the more unstable eigenvalues as the level of noise in the data increases. This is the idea behind TSVD regularization (see Section 3.4). Regardless of the underlying structure of the desired data, this approach keeps only the data that can be considered as reliable, that is, the data that can be extracted from stable eigenvectors of the data space. Such behavior can also be accomplished by using Tikhonov regularization with L equals to the identity matrix, as it was shown in Eq. (3.17). This choice of L also filters the unstable eigenvalues but using a second order filter instead of a boxcar filter as in the case of TSVD. The equivalence of the behavior is well documented in the inverse problems literature [45].

4.1.2 Choice of the offset parameter β

The parameter β, as explained in Section 3.6, is a small constant introduced as an offset to allow differentiation of the constrained least mean squares (LMS) equation for norms of the cost function smaller than or equal to 1. In order to achieve uniformity not only on β but also in the regularization parameter α, the forward model matrix and the simulated data were normalized by making their norm equal to 1. With these normalizations, there is a range of β for which the reconstructions were somewhat insensitive to the specific value of this parameter. For larger values of the regularization cost norm, the sensitivity to the value of β decreases. A value of $\beta = 10^{-7}$ was empirically selected from a set of simulations. This value is small enough so that the biased introduced in the reconstructions is not significant.

4.1.3 Choice of the regularization cost norm k

Classical Tikhonov regularization uses a quadratic cost norm ($k = 2$). As it was discussed in Chapter 3, this particular choice has the advantage of having a linear solution but is not necessarily an optimum choice in terms of performance. The regularization cost norm k was chosen by inspection of the effect of the norm on sample reconstructions. An example of the visual appearance of the reconstructions with values of k of 0.5, 1, and 2 is shown in Figure 4.3. The simulation corresponds to a reconstruction using a transducer with a bandwidth of 100%, $f_{\#}$ of 1 and ROI at the focus, with a SNR of 20 dB. This particular value of SNR was chosen because the difference in behavior is clearer when the noise in the measurementsis higher. The impact of the value of k can be summarized as follows:

- From Figure 4.3(d), for $k = 2$ the solution looks oversmoothed. Consistent with Eq. (3.17), with this choice of k the eigenvectors corresponding to the unstable eigenvalues are filtered in order to control the effect of the noise. Because the unstable eigenvalues are the ones that carry the high frequency information of the image, filtering them causes a distributed blurring which results in oversmoothed images when noise is present in the data.

- From Figure 4.3(b), for $k = 0.5$ the solution looks sparse; i.e., there is no smoothing effect on the reconstructed image at the cost of loosing many features from the original image. There is a small set of points that stand out from the rest of the pixels in the image and the overall reconstruction seems to have lost its contrast. This effect can be explained better starting from Eq. (3.22). The regularization cost function when L is chosen to be the identity matrix simplifies to $||x||_k^k$, that is, the l_k^k norm of the data to be recovered. From a first order analysis this will be accomplished with smaller values of the norm of x. Because the minimization equation is no longer linear, the eigenvalues are not filtered by only taking in consideration its particular numerical values (i.e., by using static filtering). The filtering process becomes adaptive, extracting information even from the unstable eigenvalues. This is the reason why the solution is not oversmoothed. As it was graphically shown in 3.2 that smaller values of k enforce a larger emphasis of the cost function. In this case, the sparsity implied in the l_k^k term will be larger when k is smaller.

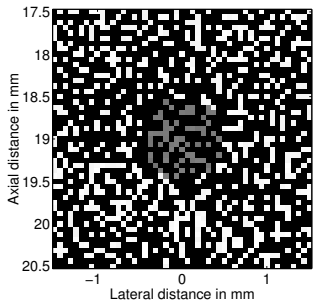

(a) Reflectivity distribution

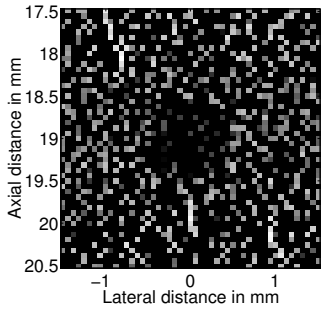

(b) k = 0.5 (MSE = 76%)

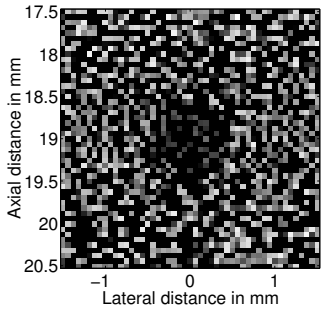

(c) k = 1 (MSE = 55%)

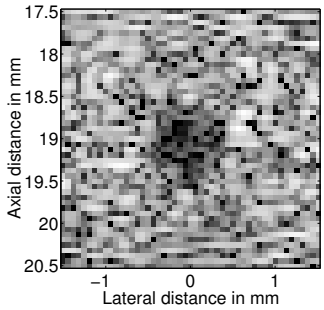

(d) k = 2 (MSE = 99%)

Figure 4.3: Effect of different choices of regularization cost norm k

- From Figure 4.3(c), for $k = 1$ a point of equilibrium between the aforementioned behaviors is achieved. The solution is somewhat sparse as in the case of $k = 0.5$ and suffers from a slight blurring which however adds visual cohesion to the image. The normalized MSE in the reconstruction with $k = 1$ (55%) is smaller than in the case of $k = 0.5$ (76%) and $k = 2$ (99%). This value of k is the one that will be used for the rest of the simulations in the present work.

4.1.4 Choice of the regularization parameter α

The most critical parameter to be chosen is the regularization parameter α, which gives the relative weight between the least mean square (LMS) term and the regularization cost function in Eq. (3.22). The effect of having a fixed value for α is shown in Figure 4.4, which shows the MSE (calculated from the data in linear scale) as a function of the SNR corresponding to the reconstruction of the reflectivity dis-

tribution of Figure 4.2(b) from pulse echo data from a simulated transducer of 100% bandwidth, $f_{\#}$ of 1 and ROI at the focus. For each value of α, the error starts on a certain level where it remains more or less constant until some threshold value of the SNR is reached. After that, the error appears to increase almost linearly with the SNR. Smaller values of α have lower values of MSE for low levels of noise (high SNR) but also lower SNR thresholds. That is, the best choice of α is data-dependent. As a complement, the reconstructed images for selected values of α of 10^{-2} and 10^{-1} and SNRs of 50 and 20 dB are also shown.

By fixing L, k, and β, a family of solutions parametrized by α is defined. As shown in Figure 4.4, the selection of the solution that extracts the largest amount of informations from the data and that is not largely distorted by noise in order to get a meaningful image is of great importance when dealing with regularization. In Section 3.7 two techniques for the automatic selection of the regularization parameter α were introduced: the L-curve and GCV. The performance of both criteria were explored for the present work and the results will be shown for each of the simulations that follow in the rest of this chapter.

The values of α were analyzed on the interval $[10^{-4}, 10^{1}]$. This interval was determined through simulations. For $\alpha < 10^{-4}$ the regularization is too weak and noise propagates to the reconstructions even for an SNR of 100 dB. For $\alpha > 10$, the regularization constraint term was large enough for the MSE in linear scale to reach asymptotic limit of 100% derived from Eq. (3.18). α was discretized using a uniform exponential grid with step size equal to 0.25, that is, $\alpha = \{10^{-4}, 10^{-3.75}, 10^{-3.5} \ \ldots \ 10^{0.75}, 10^{1}\}$.

In conclusion, for the present work the following parameters were chosen as follows:

1. The regularization matrix L will be the identity matrix.

2. The offset parameter β will be 10^{-7}.

3. The regularization cost norm k will be 1.

4. The regularization parameter α will be chosen using the L-curve and GCV on the interval $[10^{-4}, 10^{1}]$.

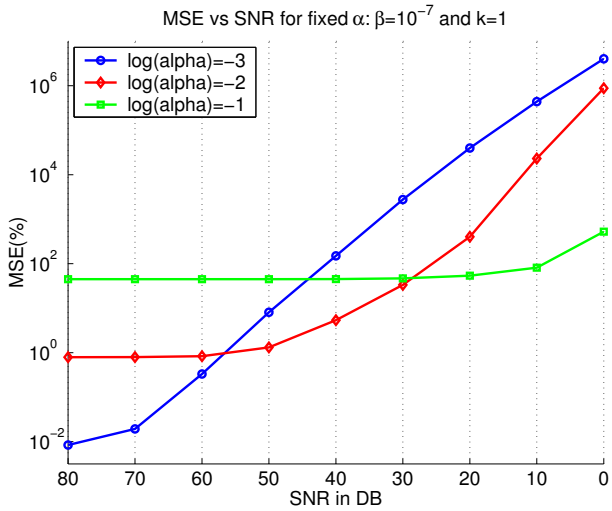

(a) MSE vs SNR for fixed α

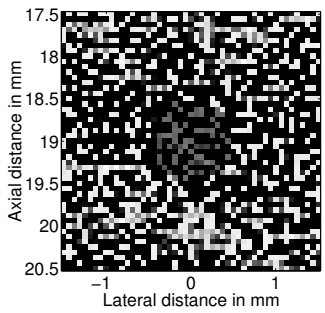

(b) $\alpha = 10^{-2}$

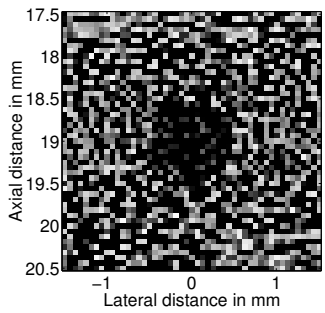

(c) $\alpha = 10^{-1}$

(1) SNR = 50 dB

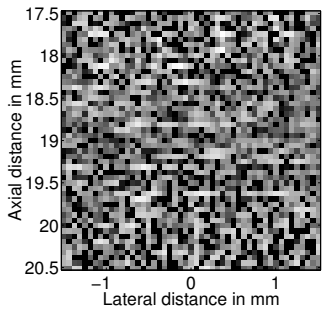

(d) $\alpha = 10^{-2}$

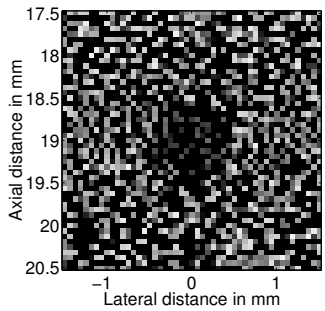

(e) $\alpha = 10^{-1}$

(2) SNR = 20 dB

Figure 4.4: Effect of different choices of regularization parameter α

For a fixed set of parameters, the tolerance for the iterative process of Eq. (3.25) was set equal to 0.001%. The factor γ was set equal to 1 because for $\gamma \leq 1$ the algorithm had a slower convergence rate with no observable reduction of the MSE.

4.2 Effect of the Bandwidth of the Transducer

The effect of the bandwidth of the transducer is analyzed by reconstructing images from data corresponding to scanning the ROIs with three simulated focused transducers with relative transmit-receive bandwidths of 100%, 50%, and 33%, respectively. The pulses in both time and frequency domain are shown in Figure 4.5. These simulations were performed with an $f_{\#}$ of 1 and thr ROI at the focus. Figure 4.6 shows the plots of the MSE as a function of the SNR for the regularization reconstructions. Figures 4.7 and 4.8 show the regularization reconstructed images selected using the L-curve for each simulated transducer for selected values of SNR of 40, 30, and 20 dB.

Several observations can be made from the results of this simulations. First, from Figure 4.6 it is clear that the error in the reconstruction increases monotonically with the level of noise in the measurements, as expected. This can also be visually verified by analyzing the quality of the images in Figures 4.7 and 4.8; the images corresponding to higher levels of SNR represent better the underlying reflectivity distribution.

Second, it can be seen that the quality of the reconstruction degrades as the bandwidth decreases. For example, for the second reflectivity distribution, for a SNR of 30 dB the normalized MSE is in the range of 20-30% for a bandwidth of 100% but the MSE increases to 90% when the bandwidth is 33%. This behavior is expected because the forward model matrix is a spatially variant convolution kernel, which is more stable if its spatial frequency content is larger. Reducing the bandwidth of the transducer will increase the axial duration of the impulse response and hence reduce the spatial frequency content in the axial direction. This will reduce the stability of the forward model and hence will increase the error of the inversion algorithm. It can also be noticed that the effect of reducing the bandwidth from 100% to 50% is very severe. This shows that the algorithm is very sensitive to the frequency content of the the ultrasonic pulse.

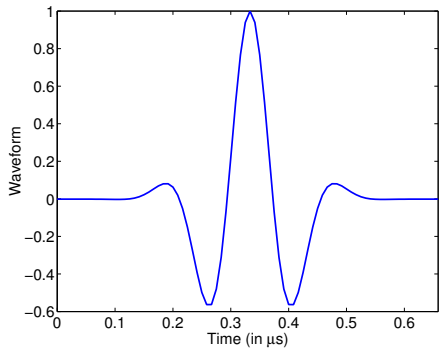

(a) Waveform

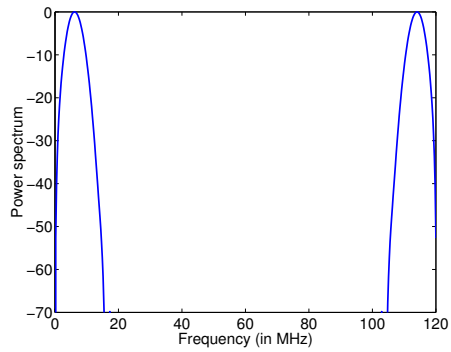

(b) Spectrum

(1) BW = 100%

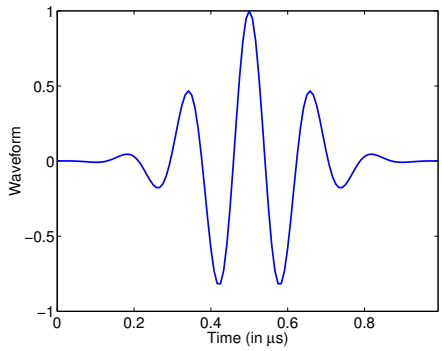

(a) Waveform

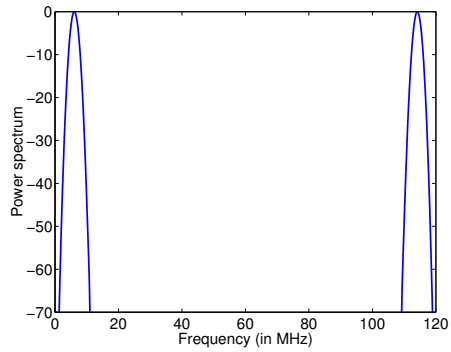

(b) Spectrum

(2) BW = 50%

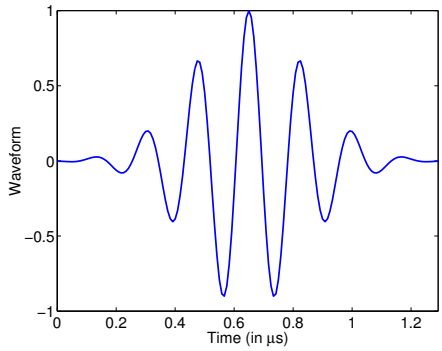

(a) Waveform

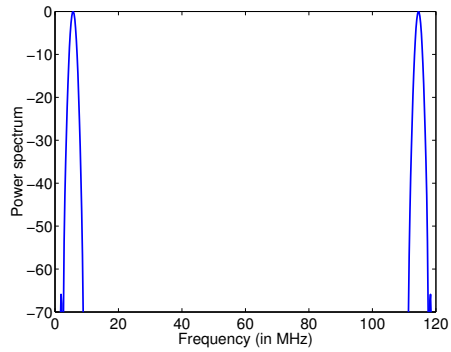

(b) Spectrum

(3) BW = 33%

Figure 4.5: Test 1 - Pulses used for the simulations

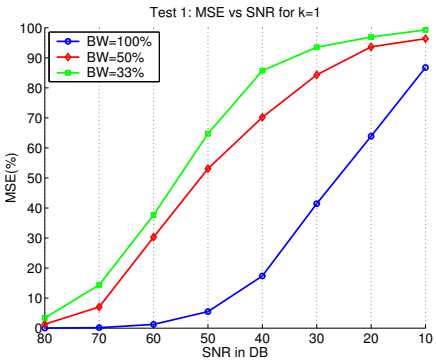

(a) First distribution

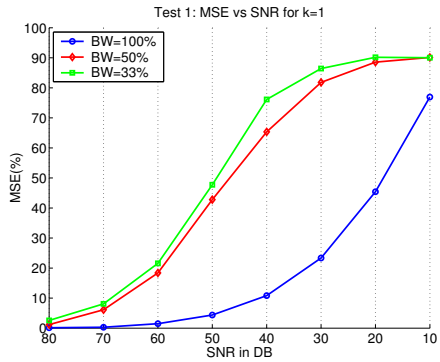

(b) Second distribution

(1) α chosen using MMSE

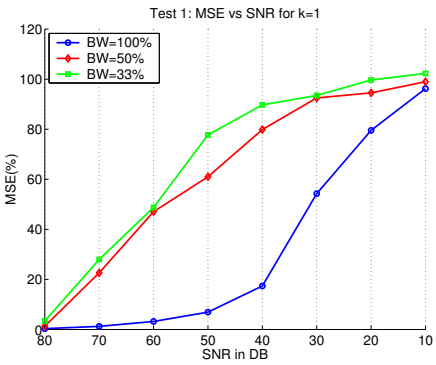

(a) First distribution

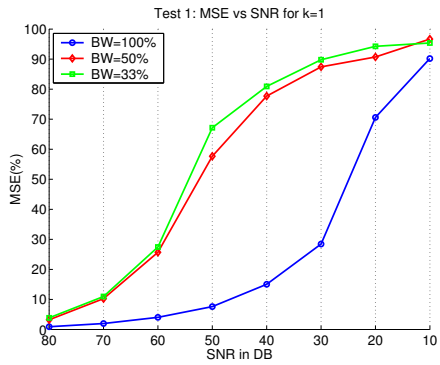

(b) Second distribution

(2) α chosen using GCV

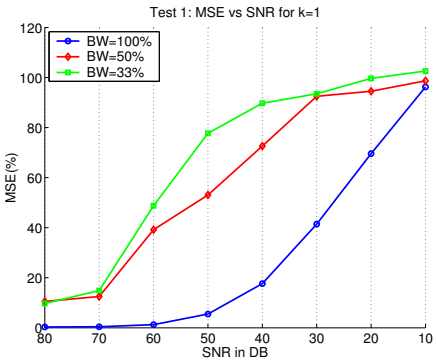

(a) First distribution

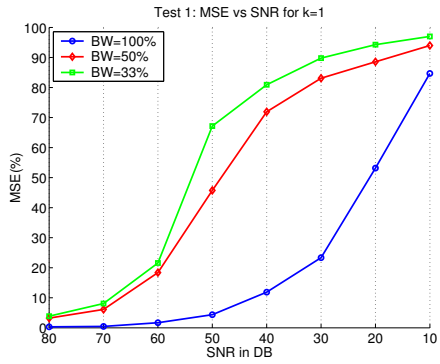

(b) Second distribution

(3) α chosen using L-curve

Figure 4.6: Test 1 - MSE curves for regularization reconstructions

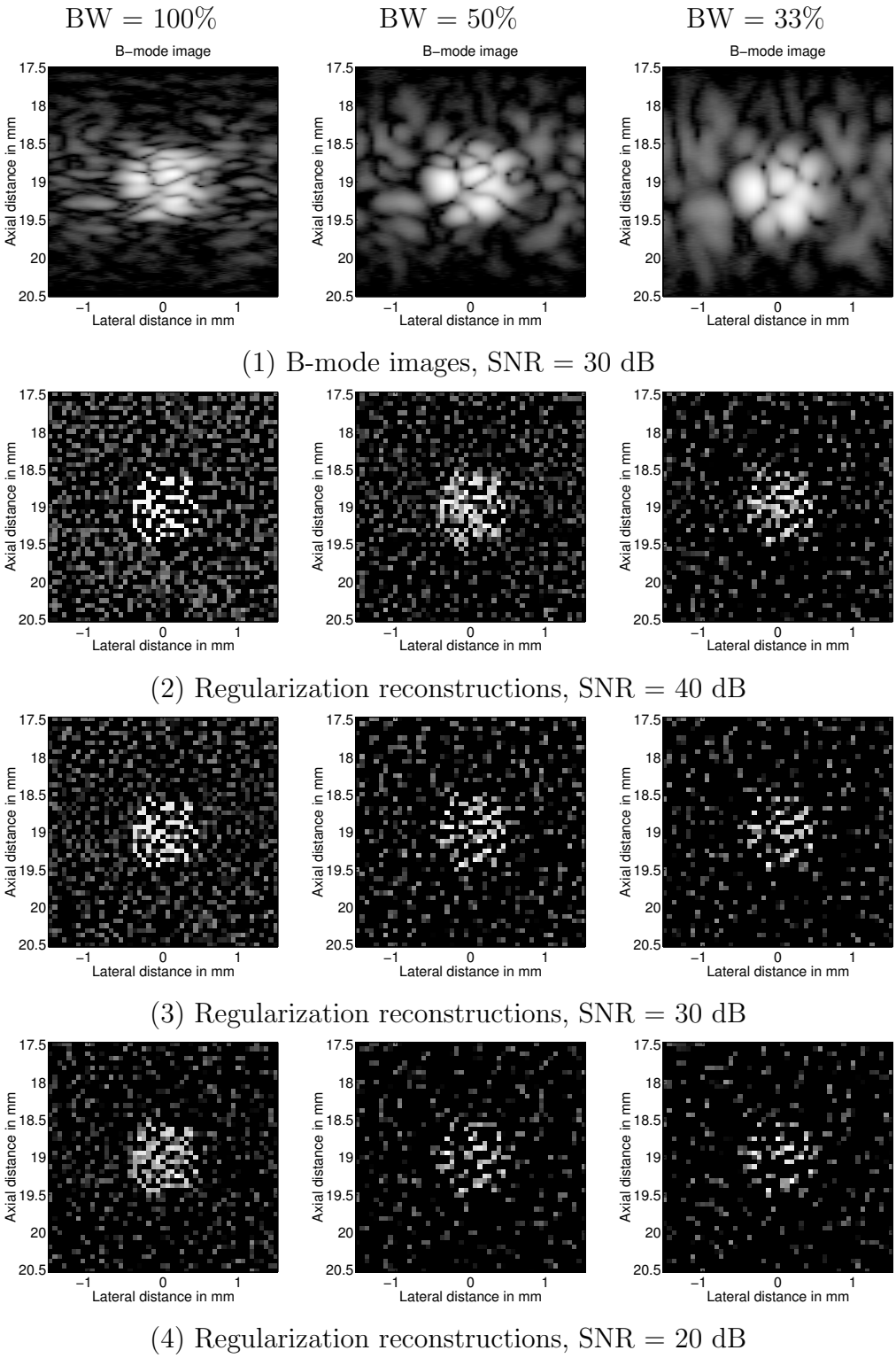

Figure 4.7: Test 1 - Reconstructed images for first reflectivity distribution selected using the L-curve

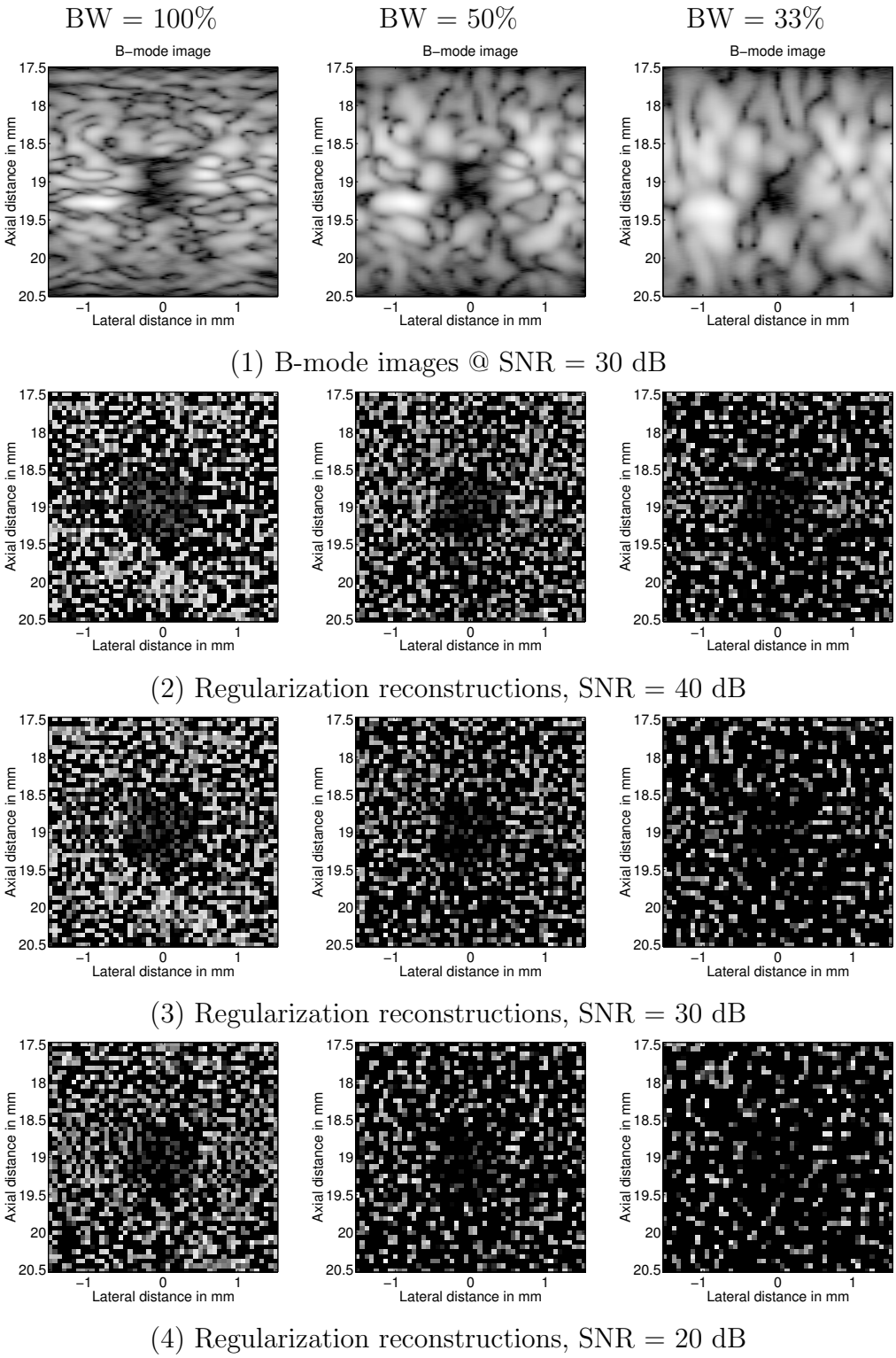

Figure 4.8: Test 1 - Reconstructed images for second reflectivity distribution selected using the L-curve

Third, the performance of the L-curve and GCV can also be analyzed from the error curves in Figure 4.6. For the reconstructions presented in this work, both techniques seem to give comparable results. A statistical analysis should be performed in order to stablish which technique has a better performance for this inverse problem. For a large range of SNRs, both techniques give reconstructions with MSEs close to the minimum attainable. Because of the similarity in the results, only the reconstructed images selected using the L-curve will be shown in the present work.

Fourth, it can be seen from the reconstructed images for SNR below 30 dB start to loose the low amplitude pixels. This is also consistent with the discussion of the effect of the regularization norm in Section 4.1. Because the chosen regularization method will penalize solutions with larger norms, the pixels of lower amplitudes will be discarded before the pixels of higher amplitudes begin to be penalized. This effect is particularly noticeable in Figure 4.7 when the SNR drops from 30 to 20 dB.

4.3 Effect of the Focal Number of the Transducer

Just like the axial resolution of the system is directly proportional to the bandwidth of the transducer, the lateral resolution at the focal region depends on the $f_{\#}$ of the transducer as given by Eq. (2.8). Hence, increasing the $f_{\#}$ should have an effect similar to decreasing its bandwidth. To test this hypothesis, another set of simulations were performed with two simulated transducers with $f_{\#}$ of 2 and 3, respectively, and the results are compared with the ones for a $f_{\#}$ of 1. The simulations were performed with a bandwidth of 100% and the ROI at the focus. The MSE versus SNR curves are shown in Figure 4.9 and reconstructed images are shown in Figures 4.10 and 4.11.

Some important observations can be derived from the results of these simulations. First, it can be noticed from visual inspection that the B-mode images in Figure 4.11 for $f_{\#}$s of 2 and 3 do not show a distinction between Region 1 and 2. This is not the case for the images reconstructed using regularization. This is a clear example of the possibility of extracting more information from the pulse-echo data than the one that can be obtained using B-mode imaging.

Second, it can be seen that the effect on the performance of the increase in focal number is not nearly as critical as the one of the reduction of the bandwidth. For example, for the second reflectivity distribution with a SNR of 30 dB, the normalized

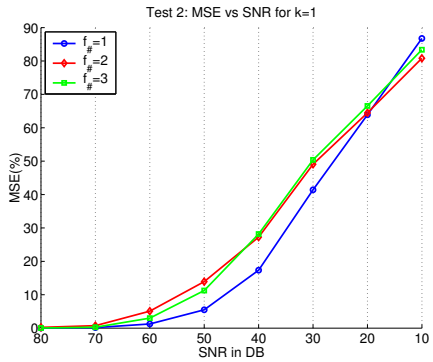

(a) First distribution

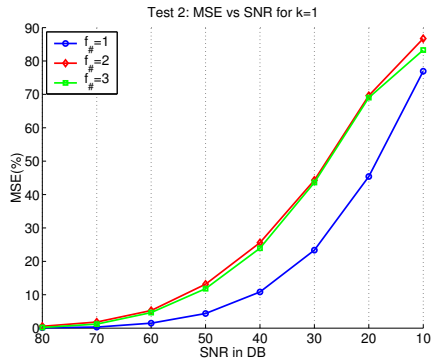

(b) Second distribution

(1) α chosen using MMSE

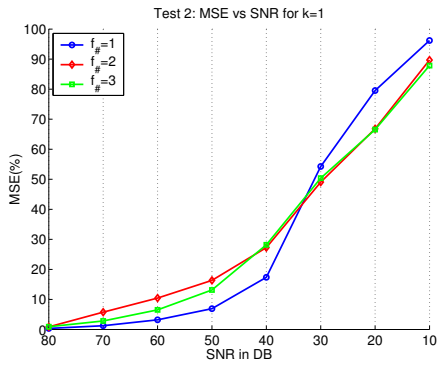

(a) First distribution

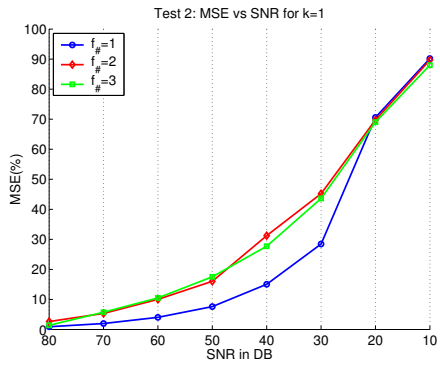

(b) Second distribution

(2) α chosen using GCV

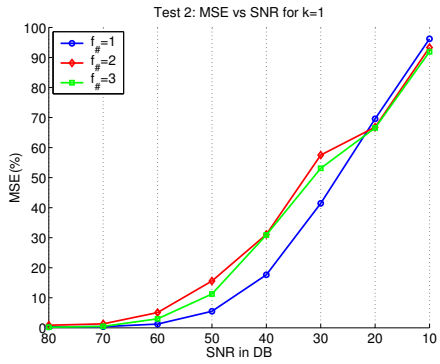

(a) First distribution

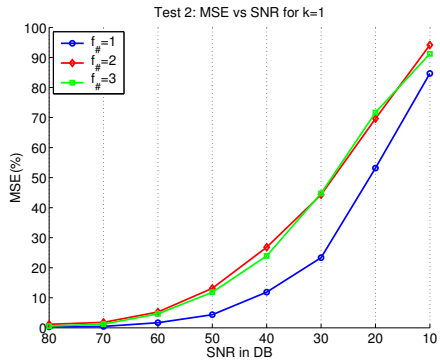

(b) Second distribution

(3) α chosen using L-curve

Figure 4.9: Test 2 - MSE curves for regularization reconstructions

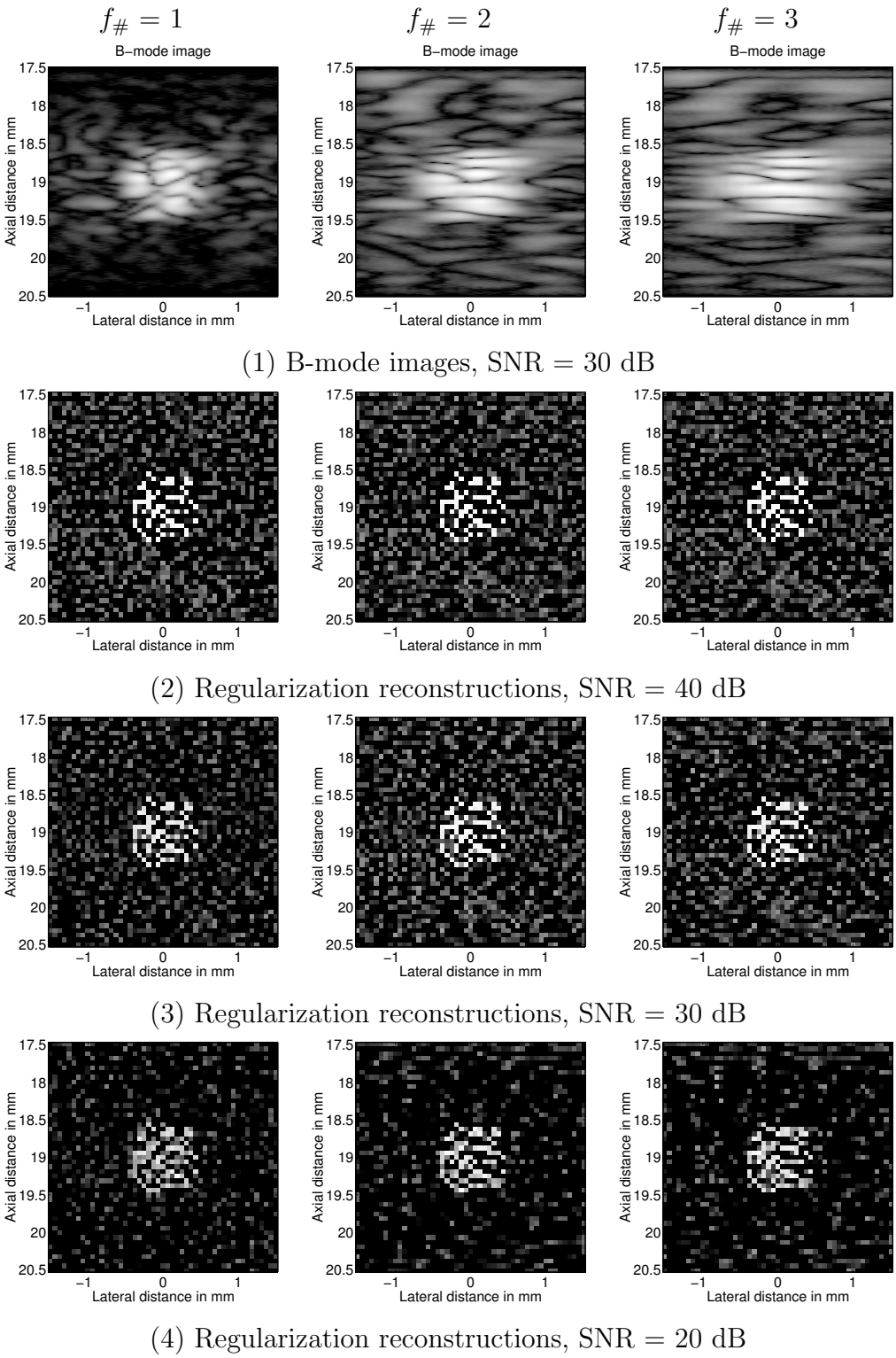

Figure 4.10: Test 2 - Reconstructed images for first reflectivity distribution selected using the L-curve

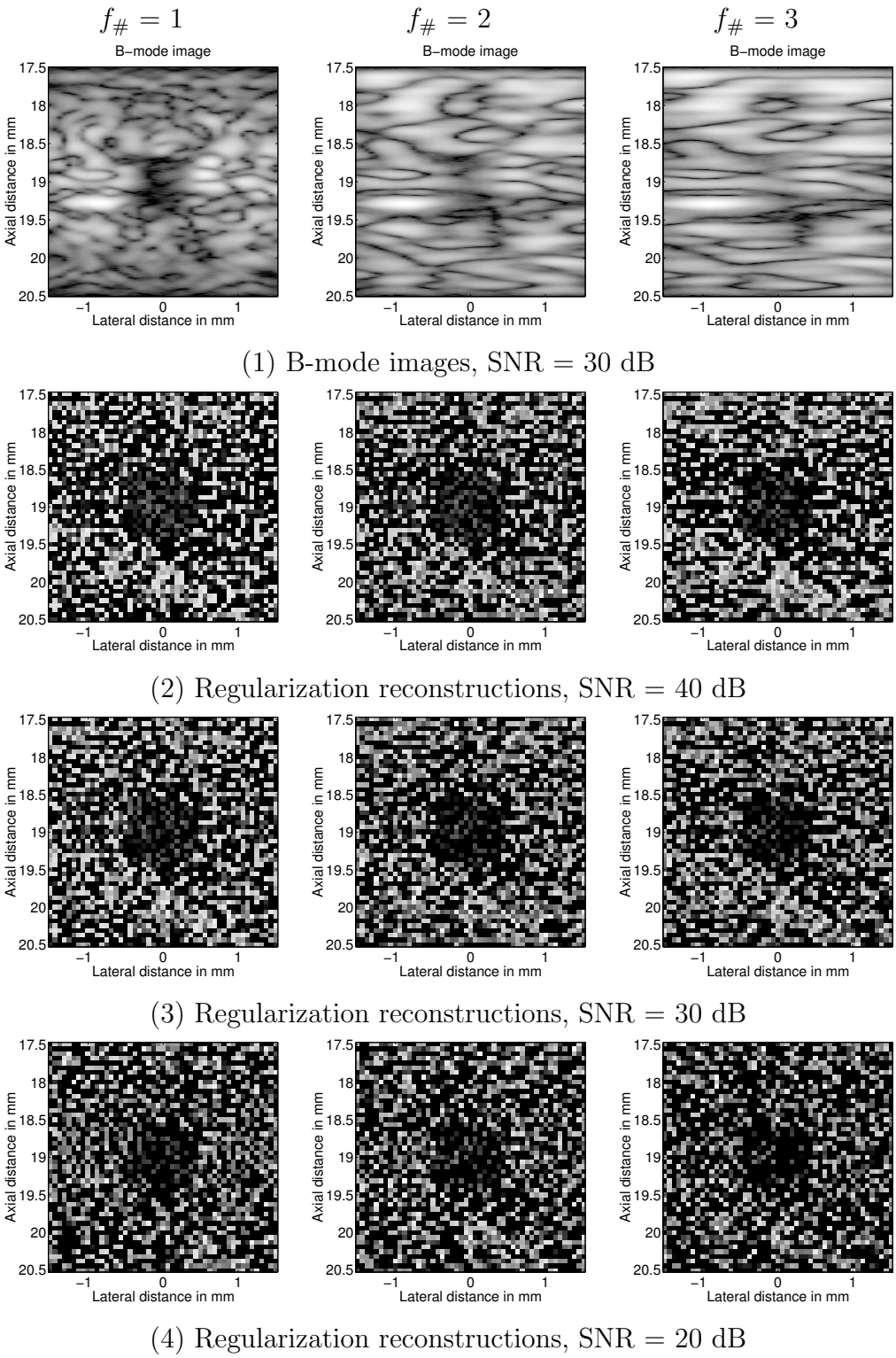

Figure 4.11: Test 2 - Reconstructed images for second reflectivity distribution selected using the L-curve

MSE increases from 20-30% to 45% when the $f_{\#}$ increases from 1 to 3. This is to be compared against the MSE of 90% for the case of a bandwidth of 33% discussed in Section 4.2. There is a couple of observations that can explain this behavior. First, the frequency content of the forward model is mostly determined by the spectrum of the acoustic pulse. Thus, the increase in $f_{\#}$ does not affect the frequency response of the forward model as severely as the reduction in the bandwidth. Second, the $f_{\#}$ affects the axial size of the focal region, as it was shown in Eq. (2.7). Even though the lateral resolution is worse, the coefficients of the forward model matrix are more uniform with variations of depth for an increased focal number, and hence there is a counteracting effect that might reduce the deterioration of the reconstructed images.

Third, Figure 4.9 shows that there seems to be an stagnation in the MSE as the focal number increases. The curves for $f_{\#}$s of 2 and 3 overlap, but the curve for an $f_{\#}$ of 1 is separated from the other two curves except for values of SNR lower than 20 dB for the first reflectivity distribution. This shows that the effect of the $f_{\#}$ on the MSE is not monotonic. This effect should be further studied. Finally, the results shown here are more qualitative than quantitative, that is, given that only one noise realization was used for each ROI, the contribution of this results is showing the trends in the reconstructions. Future work should involve reconstructing different ROIs with several noise realizations in order to have a more representative quantitative description of the problem.

4.4 Effect of the Distance of the ROI to the Focus of the Transducer

B-mode images when the ROI is out of focus suffer from loss in spatial resolution due to the beam spreading, as it was discussed in Section 2.1. Hence, it is of special interest to analyze the effect of the distance between the ROI and the focus of the transducer. For this purpose, another set of simulations was performed by using transducers with a bandwidth of 100% and an $f_{\#}$ of 1, with the ROI at 0, 2.5 and 5 mm beyond the focus of the transducer. The -6 dB depth of focus is given by Eq. (2.7); because $\lambda = 0.25$ mm and $f_{\#} = 1$, the depth of focus for these simulations is approximately 1.8 mm. This means that targets beyond 1 mm away from the focus lie outside the focal region. The reconstructed images are shown in Figure 4.12 for conventional imaging methods (B-mode and SAFT). The MSE curves are shown in

Figure 4.13 and the regularization reconstructions are shown in Figures 4.14 and 4.15.

Some observations can be made from the results. First, it can be seen from Figure 4.12 that the B-mode images are of very poor quality when the ROI is beyond the focus of the transducer, as expected. SAFT processing is able to improve the quality of the image when compared to the unfocused B-mode images, but only to a limited extent because of the presence of sidelobes. This phenomenon was explored in the theoretical development of SAFT in Section 2.2.1. Also, in order to successfully apply SAFT algorithms, the sampling aperture should satisfy Shannon's theorem [38], which states that there is a minimum coverage of the ROI needed in order to have enough data and avoid aliasing. Because the number of A-Scans was held constant for all cases, Shannon's theorem is not satisfied for large distances and the intensity level and size of the sidelobes increase. For the image corresponding to the second reflectivity distribution there is not a clear distinction between the concentric regions that conform the ROI. The distortion due to the sidelobes increases with the distance between the ROI and the focus of the transducer.

Second, the effect of the distance between ROI and the focus of the transducer on the MSE is not as critical as the effect of the bandwidth as it can be seen from Figure 4.13. Taking again as a reference the second reflectivity distribution and an SNR of 30 dB, the MSE increases only from 20-30% to 35%. In fact, there is an overlapping of several of the MSE curves shown in Figure 4.13. For the second reflectivity distribution, there is an average separation of 5-10% in the MSE achieved when the ROI is at the focus compared to the unfocused cases; the MSE curves for 2.5 and 5 mm however are overlapping. In fact, for the second distribution, there are values of the SNR below 30 dB for which a smaller MSE is achieved for a distance of 5 mm than for 2.5 mm. This can be explained because the pulse-echo data corresponding to the unfocused cases contain information on the frequency domain comparable to the one from the focused scenario. The frequency information is contained on the pulse-echo data but spreaded over the frequency region of support of the imaging system. SAFT is only able to retrieve the information to a limited extent. The reconstruction using regularization appears to be much more efficient in the task of extracting the information from the pulse-echo data. The limiting factor on the performance of the reconstructions, as in the other simulations, is the amount of noise in the measurements.

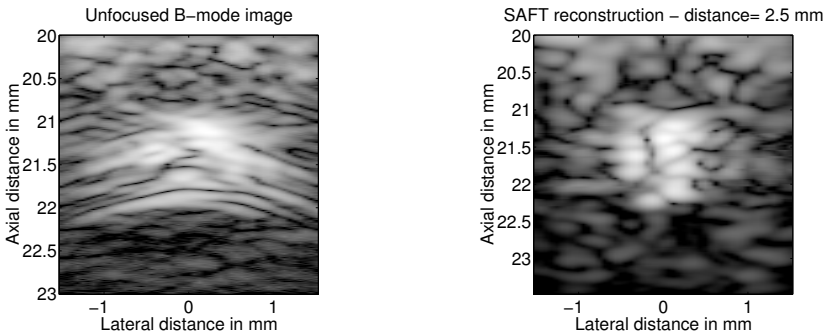

(1) First refectivity distribution, distance = 2.5mm

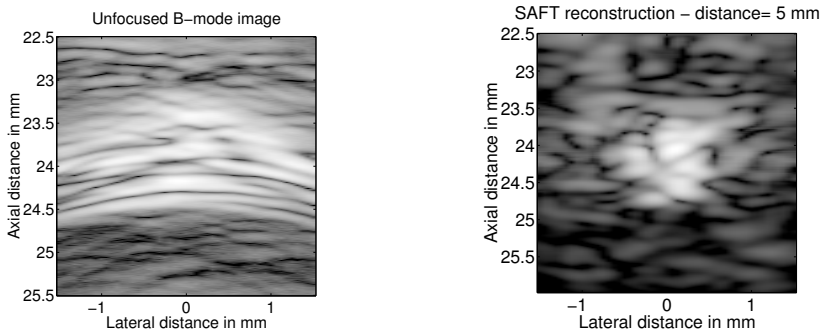

(2) First refectivity distribution, distance = 5mm

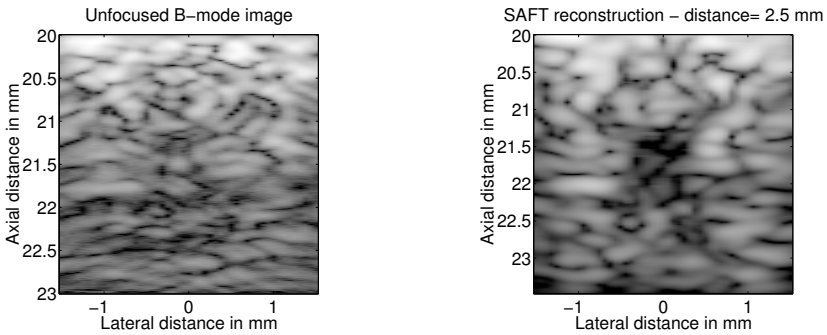

(3) Second refectivity distribution, distance = 2.5mm

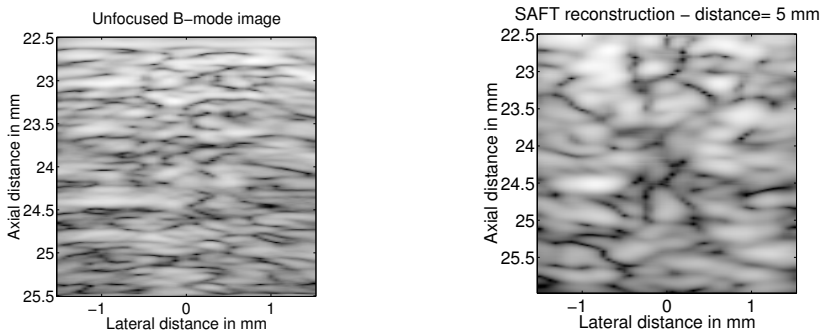

(4) Second refectivity distribution, distance = 5mm

Figure 4.12: Test 3 - Conventional images for out of focus cases

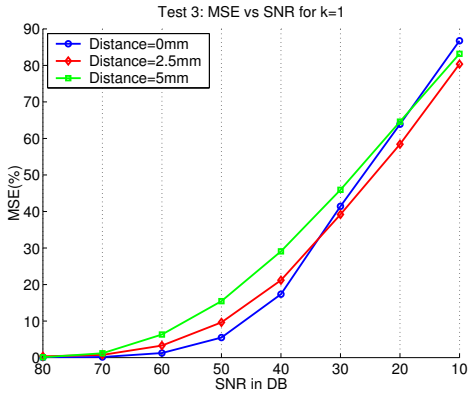

(a) First distribution

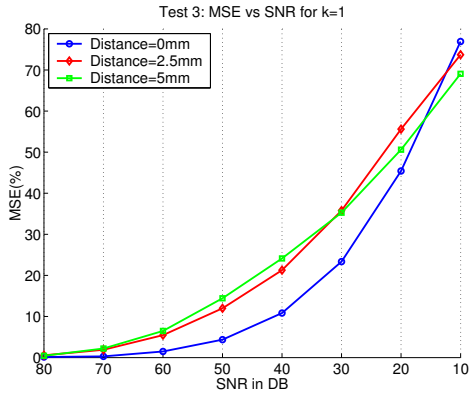

(b) Second distribution

(1) α chosen using MMSE

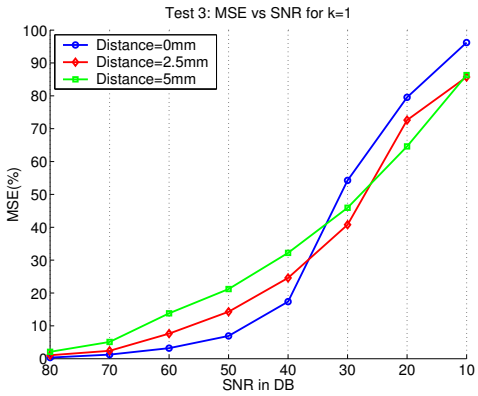

(a) First distribution

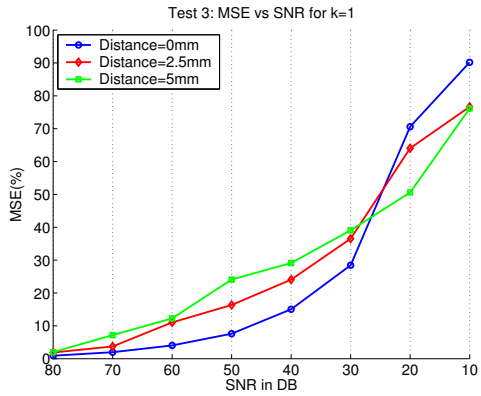

(b) Second distribution

(2) α chosen using GCV

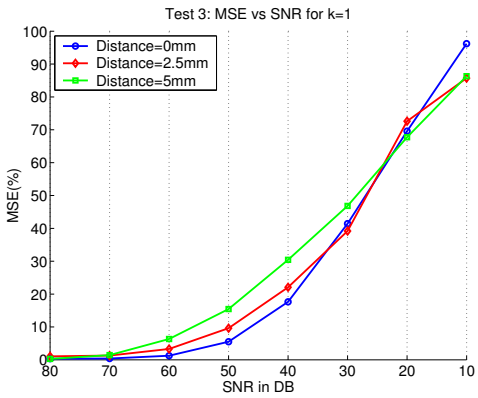

(a) First distribution

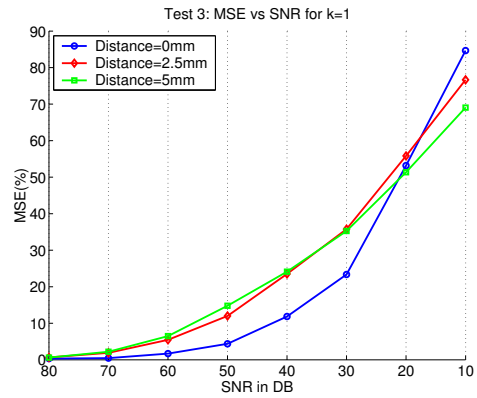

(b) Second distribution

(3) α chosen using L-curve

Figure 4.13: Test 3 - MSE curves for regularization reconstructions

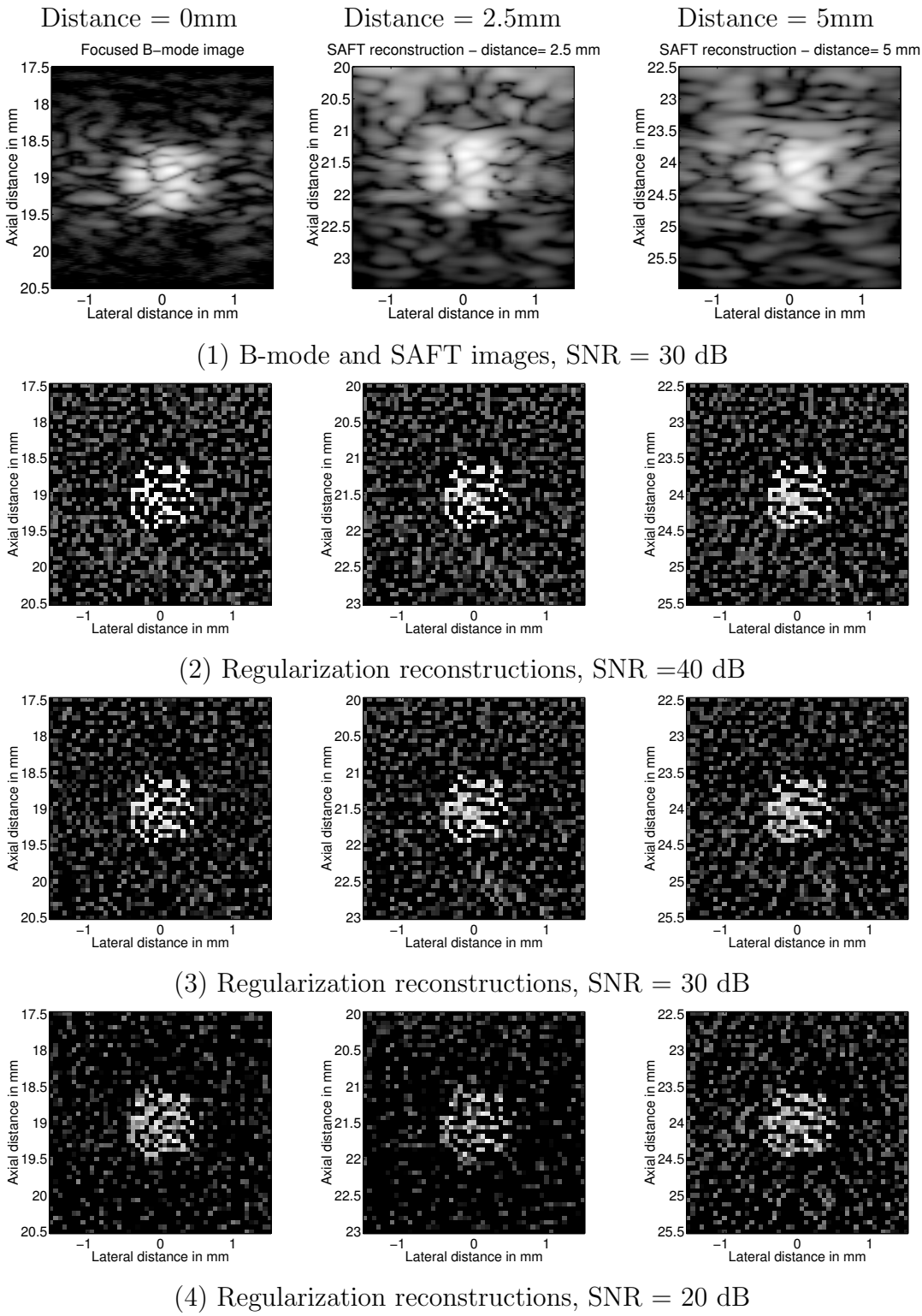

Figure 4.14: Test 3 - Reconstructed images for first reflectivity distribution selected using the L-curve

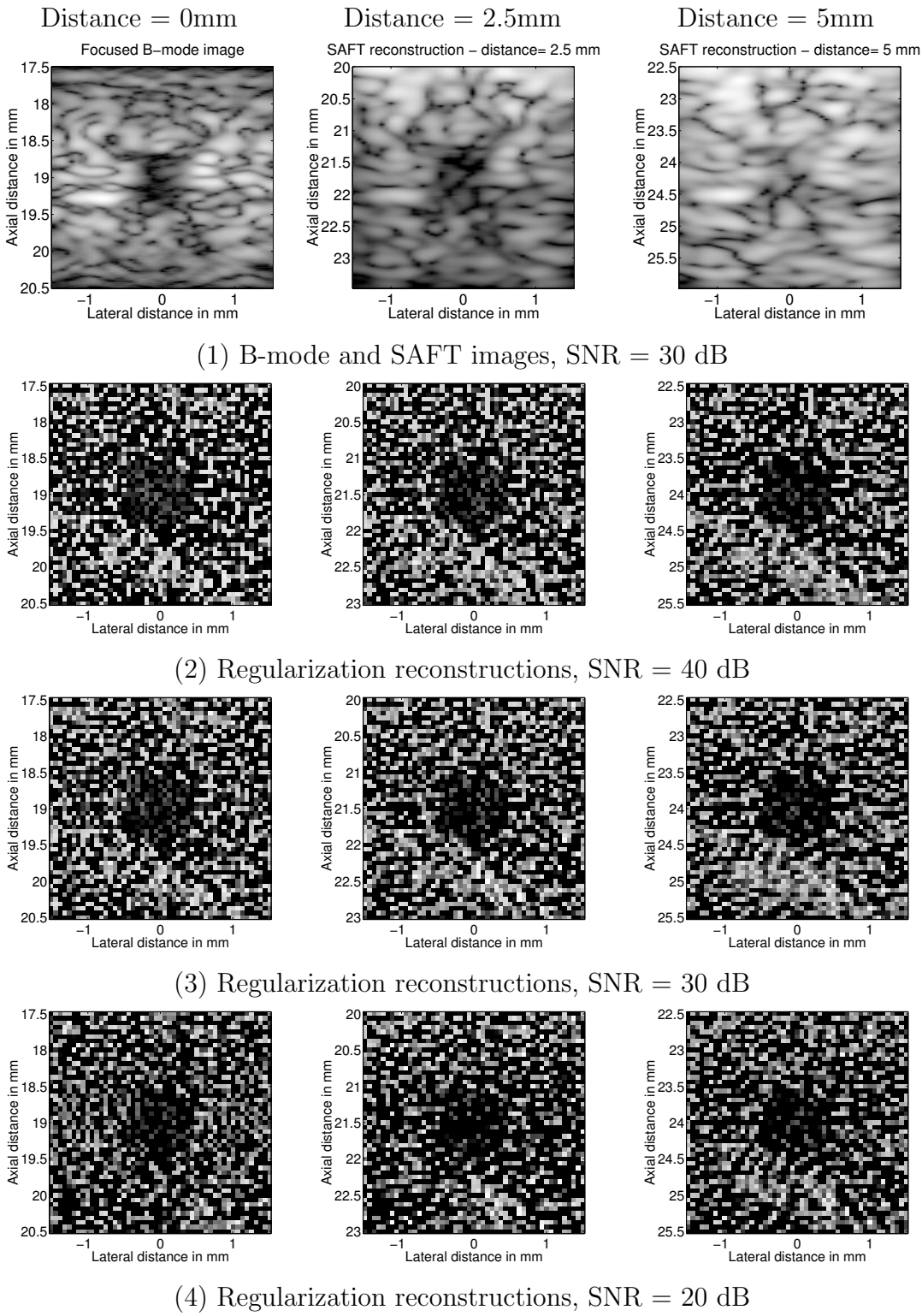

Figure 4.15: Test 3 - Reconstructed images for second reflectivity distribution selected using the L-curve

This concludes the presentation of the results of the simulations performed for the present work. The effect of parameters of both the regularization algorithm and the imaging system (bandwidth, $f_{\#}$ and distance between ROI and the focus of the transducer) were analyzed to explore the feasibility and effectiveness of regularization reconstruction. In the next chapter, a closing discussion about the results will be presented, together with suggestions for future work directions.

CHAPTER 5

CONCLUSIONS AND FUTURE WORK

5.1 Conclusions

The performance of conventional imaging techniques such as B-mode and SAFT is mainly limited by the size of the resolution cell of the imaging system. For monostatic imaging with a focused transducer, the spatial resolution depends on the wavelength, bandwidth and $f_{\#}$ when the ROI is at the focus. When the ROI is out of focus, the lateral resolution becomes worse because of the beam spreading due to diffraction. The goal of this study was to analyze if regularization approaches are a feasible alternative to conventional imaging techniques.

It was found from the simulations that more information can be extracted from the pulse-echo data using inverse problems and regularization approaches compared to conventional techniques when the SNR is high. However, as the noise in the measurements increases, the MSE of the reconstructions also increases and the quality of the reconstruction degrades because of excesive amplification of the measurement noise during the inversion process. This mechanism of image distortion is not present in conventional imaging techniques.

The size of the resolution cell of the imaging system also has an impact on the performance of regularization techniques by determining the lower threshold for the SNR for which these approaches yield an image of better quality. This is a direct result of a lower spatial frequency content of the forward model which results in a more unstable inverse problem. A larger bandwidth result in better performance as measured by the MSE for fixed SNR. The $f_{\#}$ and the distance between the ROI and the focus do not necessarily have a monotonic effect on the quality of the reconstruction as measured by the MSE. The optimum reconstruction for the simulations occurred for a bandwidth of 100%, $f_{\#}$ of 1 and ROI at the focus. For these settings and for values of SNR below 20 dB, several of the image features were lost during the reconstruction process in order to control the distortion due to the noise.

From the simulation results in Chapter 4, it was concluded that the bandwidth has the largest effect on the MSE, followed by the $f_{\#}$. The distance between the ROI and the focus of the transducer had the lowest effect. In fact, the corresponding MSE curves overlap for low values of SNR.

5.2 Future Work

5.2.1 Statistical analysis of the problem

As it has been stated in Chapter 4, it is of special interest to perform several reconstructions with the same settings used in the present work, using different noise realizations and possibly different ROIs with the same scatterer density per resolution cell, in order to have an statistically meaningful evaluation of the effect of the $f_{\#}$ and the distance between the ROI and the focus.

5.2.2 Changes in the simulation setup

The simulation setup used for this work was only chosen for simplicity in the formulation of the problem, in order to understand the limitations of the inversio process using regularization techniques. There are two factors that limit the effectiveness of the inversion:

1. The noise in the measurements. In order to discriminate and better compensate for the noise, more measurements can be used for the same amount of unknowns. This can be achieved in at least a couple of ways:

    - The average of several measurements with the same configuration used in the present work can be used instead of a single set of measurements. For uncorrelated, zero-mean additive noise that would result in a reduction of the noise variance and hence an improvement on the SNR. However, this approach has two drawbacks: first, there is an increment in the acquisition time, and second, in certain imaging situations (such as biomedical imaging) the ROI is not stationary, so both the noiseless data and the noise change with each measurement.

    - Instead of using a monostatic configuration, more than one receiver can be used for each transmission [56],[57]. This has the advantage of providing more measurements for every transmission. Related research topics are

the determination of the number and spatial distribution of the receivers needed to achieve an optimum reconstruction.

2. The size of the resolution cell. From the analysis in Chapter 4 it was concluded that the bandwith is the limiting physical factor in the reconstructions. To overcome this, a series of transducers with different frequency bands can be used as in [20].

5.2.3 Changes in the reconstruction algorithm

The choice of the regularization algorithm has also an impact on the performance of the reconstructions. Even by fixing the regularization method to be generalized Tikhonov, more variants can be explored. For example, region-based regularization cost terms can be added to the minimization problem used for the reconstructions. An expected trade-off is a decrease in the MSE versus an increase in the contrast of the reconstructions for low values of SNR when compared to the regularization cost used for this work. A combination of region-based and identity cost terms have been successfully used in radar imaging [25]. An inmediate problem in using more than one regularization cost term is the need to determine more than one regularization parameter α, so that multidimensional versions of the parameter selection techniques are needed. This topic has been addressed in other works, such as [58] for multidimensional GCV and [59] for multidimensional L-curve.

5.2.4 Effect of the grid

With every discretization problem there is a tradeoff involving the size of the grid to use. A very coarse grid will result in a bad representation of the continuous measured field and the fit to the measured data will be poor. There is an improvement as the grid becomes finer up to a certain limit, because the measured data does not contain enough information to resolve features beyond a certain limit. As a result, the inverse problem becomes more unstable because it becomes too overdetermined. Hence, there exists an optimum sampling grid that depends on the forward model. A recent example involving grid size selection in inverse problems using regularization can be found in [60].

5.2.5 Matrix-free solution to the problem

A problem with the inverse problem formulation used in the present work is the computational cost of the algorithm. The simulations of Chapter 4 were run on a dual processor Opteron 248 computer with a 2.26 GHz clock and 4 GB of memory running on Linux Fedora Core 2. For the 49 by 49 images used in the simulations, the inversion took an average of 60 iterations to converge for fixed regularization parameters. The inversion algorithm was coded on Matlab version 6.1. Each iteration took 3.8 seconds for a total average time of 228 seconds using 7% of the available memory. However, the computation time and memory usage increase with the number of unknowns. For an image of n by m pixels, the size of the matrices used for the inversion process is $(nm)^2$. Doubling the size of the image in both dimensions, that is, reconstructing an image of roughly 100 by 100 pixels, would demand an increase in the size of the matrices by a factor of 16. Even though the sparcity of the inverse operator increases with the size of the ROI due to the finite size of the resolution cell, it can be easily seen that a matrix formulation is not efficient in term of memory management, which imposes a limit on the number of unknowns that can be solved. This problem is of special importance because for real imaging scenarios the ROI is three-dimensional, which increases the dimensionality of the problem. To overcome this limitation, regularized iterative matrix-free formulations can be used. Distributed approaches for large matrix-free equation systems have been reported to solve for even millions of unknowns [61]. Related research topics involve the study of the convergence of the iterative algorithm as in [62].

5.2.6 Changes in the forward model

The effect of modelling errors have also to be considered. Several simplifications were assumed for the present work, i.e., the speed of sound was assumed to be homogeneous, attenuation and non-linear propagation were not considered, and multiple reflections were neglected. In order to apply this algorithm in a real imaging scenario, the impact of all of these items have to be studied. More than quantifying the distortion that this simplifications generate for real data, it is of special interest to incorporate them into the forward model. For example, it is a well known fact that the quality of SAFT and array imaging degrades because of phase aberration [63] due to inhomogeneities in the speed of sound. The feasibility of using inverse problems approaches to solve for this particular issue is a relevant topic of future research.

REFERENCES

[1] C. F. Schueler, H. Lee, and G. Wade, "Fundamentals of digital ultrasonic imaging," *IEEE Transactions on Sonics and Ultrasonics*, vol. 31, no. 4, pp. 195–217, July 1984.

[2] M. Schickert, M. Krause, and W. Muller, "Ultrasonic imaging of concrete elements using reconstruction by synthetic aperture focusing technique," *Journal of Materials in Civil Engineering*, vol. 15, no. 3, pp. 235–246, May/June 2003.

[3] S. Mahaut, J. Godefroit, O. Roy, and G. Cattiaux, "Application of phased array techniques to coarse grain components inspection," *Ultrasonics*, vol. 42, nos. 1-9, pp. 791–796, April 2004.

[4] H. Berndt, A. P. Schniewind, and G. C. Johnson, "High-resolution ultrasonic imaging of wood," *Wood Science and Technology*, vol. 33, no. 3, pp. 185–198, June 1999.

[5] E. Brusseau, C. L. de Korte, F. Mastik, J. Schaar, and A. F. W. Van der Steen, "Fully automatic luminal contour segmentation in intracoronary ultrasound imaging - a statistical approach," *IEEE Transactions on Medical Imaging*, vol. 23, no. 5, pp. 554–566, May 2004.

[6] M. Vogt, S. Scharenberg, R. Scharenberg, K. Hoffmann, P. Altmeyer, and H. Ermert, "In vivo evaluation and imaging of skin elasticity applying high frequency (22 MHz) ultrasound," in *IEEE Ultrasonics Symposium*, 2002, pp. 1863–1866.

[7] M. L. Oelze, W. D. O'Brien, Jr., J. P. Blue, and J. F. Zachary, "Differentiation and characterization of rat mammary fibroadenomas and 4T1 mouse carcinomas using quantitative ultrasound imaging," *IEEE Transactions on Medical Imaging*, vol. 23, no. 6, pp. 764–771, June 2004.

[8] S. L. Bridal, J. Correas, A. Saied, and P. Laugier, "Milestones on the road to higher resolution, quantitative, and functional ultrasonic imaging," in *Proceedings of the IEEE*, vol. 91, no. 10, October 2003, pp. 1543–1561.

[9] R. E. Blahut, *Theory of Remote Image Formation.* Cambridge, MA : Cambridge University Press, 2004.

[10] G. S. Kino, *Acoustic Waves: Devices, Imaging, and Analog Signal Processing.* Englewood Cliffs, NJ : Prentice Hall, 1987.

[11] A. D. Pierce, *Acoustics: An Introduction to its Physical Principles and Applications.* Woodbury, NY : Acoustical Society of America, 1989.

[12] L. E. Kinsler, A. R. Frey, A. B. Coppens, and J. V. Sanders, *Fundamentals of Acoustics.* New York, NY : Wiley, 2000.

[13] C. H. Frazier, "Synthetic aperture focusing technique using a virtual transducer element source," M.S. thesis, University of Illinois at Urbana-Champaign, 1996.

[14] A. Macovski, "Ultrasonic imaging using arrays," in *Proceedings of the IEEE*, vol. 67, no. 4, April 1979, pp. 484–495.

[15] C. H. Frazier, "A two-dimensional amplitude-steered array for real-time volumetric acoustic imaging," Ph.D. dissertation, University of Illinois at Urbana-Champaign, 2000.

[16] S. I. Nikolov, J. A. Jensen, R. Dufait, and A. Schoisswohl, "Three-dimensional real-time synthetic aperture imaging using a rotating phased array transducer," in *IEEE Ultrasonics Symposium*, 2002, pp. 1585–1588.

[17] C. B. Burckhard, "Speckle in ultrasound B-mode scans," *IEEE Transactions on Sonics and Ultrasonics*, vol. 25, no. 1, pp. 1–6, January 1978.

[18] R. F. Wagner, S. W. Smith, J. M. Sandric, and H. Lopez, "Statistics of speckle in ultrasound B-scans," *IEEE Transactions on Sonics and Ultrasonics*, vol. 30, no. 3, pp. 153–163, May 1983.

[19] F. Lingvall, T. Olofsson, and T. Stepinski, "Synthetic aperture imaging using sources with finite aperture: Deconvolution of the spatial impulse response," *Journal of the Acoustical Society of America*, vol. 114, no. 1, pp. 225–234, July 2003.

[20] E. Ayme-Bellegarda and T. Habashi, "Ultrasonic inverse scattering of multi-dimensional objects buried in multilayer elastic background structures," *IEEE Transactions on Ultrasonics, Ferroelectrics and Frequency Control*, vol. 39, no. 1, pp. 11–18, January 1992.

[21] H. Desoky, A. B. M. Youssef, and Y. M. Kadah, "Reconstruction using optimal spatially variant kernel for B-mode ultrasound imaging," in *SPIE Medical Imaging 2003: Ultrasonic Imaging and Signal Processing*, 2003, pp. 147–153.

[22] C. Liu, Y. Wang, and P. A. Heng, "A comparison of truncated total least squares with Tikhonov regularization in imaging by ultrasound inverse scattering," *Physics in Medicine and Biology*, vol. 48, no. 15, p. 24372451, August 2003.

[23] X. Zhang and S. Broschat, "A comparison of material classification techniques for ultrasound inverse imaging," *Journal of the Acoustical Society of America*, vol. 111, no. 1, pp. 457–467, January 2002.

[24] H. Feng, D. Castanon, and W. C. Karl, "Underground imaging based on edge-preserving regularization," in *IEEE International Conference on Intelligence, Information and Systems*, 1999, pp. 460–464.

[25] W. C. Karl and M. Cetin, "Feature-enhanced synthetic aperture radar image formation based on nonquadratic regularization," *IEEE Transactions on Image Processing*, vol. 10, no. 4, pp. 623–631, April 2001.

[26] D. M. Malioutov, "A sparse signal reconstruction perspective for source localization with sensor arrays," M.S. thesis, Massachusetts Institute of Technology, 2003.

[27] P. Charbonnier, L. Blanc-Feraud, G. Aubert, and M. Barlaud, "Deterministic edge-preserving regularization in computed imaging," *IEEE Transactions in Image Processing*, vol. 6, no. 2, pp. 298–311, February 1997.

[28] A. Delaney and Y. Bresler, "Globally convergent edge-preserving regularized reconstruction: An application to limited-angle tomography," *IEEE Transactions on Image Processing*, vol. 7, no. 2, pp. 204–221, February 1998.

[29] A. Jarrot, H. Liebgott, P. Delachartre, and M. Robini, "Edge-preserving image reconstruction for Young's modulus recovery from ultrasonic data," in *IEEE Ultrasonics Symposium*, 2003, pp. 1919–1922.

[30] Z. Mu, R. Plemmons, and P. Santago, "Iterative ultrasonic signal and image deconvolution for estimation of the complex medium response," *IEEE Transactions on Ultrasonics, Ferroelectronics and Frequency Control*, submitted for publication.

[31] Z. Mu, R. Plemmons, D. Herrington, and P. Santago, "Estimation of complex ultrasonic medium responses by deconvolution," in *IEEE International Symposium on Biomedical Imaging. Proceedings.*, July 2002, pp. 1047–1050.

[32] D. Mumphord and J. Shah, "Boundary detection by minimizing functionals," in *IEEE Conference in Computer Vision and Pattern Recognition*, 1985, pp. 22–26.

[33] W. C. Karl and M. Cetin, "Edge preserving image reconstruction for coherent imaging applications," in *IEEE International Conference on Image Processing*, 2002, pp. 481–484.

[34] U. Amato and W. Hughes, "Maximum entropy regularization of Fredholm integral equations of the first kind," *lnverse Problems*, vol. 7, no. 6, pp. 793–808, December 1991.

[35] B. Borden, "Maximum entropy regularization in inverse synthetic aperture radar imagery," *IEEE Transactions in Signal Processing*, vol. 40, no. 4, pp. 969–973, April 1992.

[36] J. Krautkramer and H. Krautkramer, *Ultrasonic Testing of Materials.* New York, NY : Springer-Verlag, 1989.

[37] R. L. Visentin, "A digital signal processing view of strip-mapping synthetic aperture radar," M.S. thesis, University of Illinois at Urbana-Champaign, 1988.

[38] M. Soumekh, *Synthetic Aperture Radar Signal Processing with Matlab Algorithms.* New York, NY : Wiley, 1999.

[39] J. Curlander and R. McDonough, *Synthetic Aperture Radar: Systems and Signal Processing.* New York, NY : Wiley, 1991.

[40] C. Passmann and H. Ermert, "A 100 MHz ultrasound imaging system for dermatologic and ophthalmologic diagnostics," *IEEE Transactions on Ultrasonics, Ferroelectrics and Frequency Control*, vol. 43, no. 4, pp. 545–552, July 1996.

[41] J. A. Jensen and N. B. Svendsen, "Calculation of pressure fields from arbitrarily shaped, apodized, and excited ultrasound transducers," *IEEE Transactions on Ultrasonics, Ferroelectrics and Frequency Control*, vol. 39, no. 2, pp. 262–267, March 1992.

[42] K. Raum and W. D. O'Brien, Jr., "Pulse-echo field distribution measurement technique for high-frequency ultrasound sources," *IEEE Transactions on Ultrasonics, Ferroelectrics and Frequency Control*, vol. 44, no. 4, pp. 810–815, July 1997.

[43] D. S. Watkins, *Fundamentals of Matrix Computations.* New York, NY : Wiley, 2002.

[44] P. C. Hansen, *Rank-Deficient and Discrete Ill-Posed Problems : Numerical Aspects of Linear Inversion.* Philadelphia, PA : SIAM, 1988.

[45] H. W. Engl, M. Hanke, and A. Neubauer, *Regularization of Inverse Problems.* Boston, MA : Kluwer Academic Publishers, 1996.

[46] C. R. Vogel, *Computational Methods for Inverse Problems.* Philadelphia, PA : SIAM, 2002.

[47] A. Bovik, *Handbook of Image and Video Processing.* San Diego, CA : Academic Press, 2000.

[48] V. A. Morozov, "On the solution of functional equations by the method of regularization," *Soviet Mathematics - Doklady*, vol. 7, pp. 414–417, 1966.

[49] C. L. Lawson and R. J. Hanson, *Solving Least Squares Problems.* Philadelphia, PA : Prentice-Hall, 1974.

[50] P. C. Hansen, "Analysis of discrete ill-posed problems by means of the L-curve," *SIAM Review*, vol. 34, no. 4, pp. 561–580, December 1992.

[51] S. Oraintara, W. C. Karl, D. A. Castanon, and T. Q. Nguyen, "A method for choosing the regularization parameter in generalized Tikhonov regularized linear inverse problems," in *2000 International Conference on Image Processing*, September 2000, pp. 93–96.

[52] C. R. Vogel, "Non-convergence of the L-curve regularization parameter selection method," *Inverse Problems*, vol. 12, no. 4, pp. 535–547, August 1996.

[53] M. E. Kilmer and D. P. O'Leary, "Choosing regularization parameters in iterative methods for ill-posed problems," *SIAM Journal of Matrix Analysis and Applications*, vol. 22, no. 4, p. 12041221, April 2001.

[54] G. H. Golub, M. Heath, and G. Wahba, "Generalized cross-validation as a method for choosing a good ridge parameter," *Technometrics*, vol. 21, pp. 215–223, 1979.

[55] T. A. Tuthill, R. H. Sperry, and K. J. Parker, "Deviations from Rayleigh statistics in ultrasonic speckle," *Ultrasonic Imaging*, vol. 10, no. 2, pp. 81–89, April 1988.

[56] J. Shen and E. S. Ebbini, "A new coded-excitation ultrasound imaging system - Part I: Basic principles," *IEEE Transactions on Ultrasonics, Ferroelectrics and Frequency Control*, vol. 43, no. 1, pp. 131–140, January 1996.

[57] J. Shen and E. S. Ebbini, "A new coded-excitation ultrasound imaging system - Part II: Operator design," *IEEE Transactions on Ultrasonics, Ferroelectrics and Frequency Control*, vol. 43, no. 1, pp. 141–148, January 1996.

[58] M. D. Butala, "Three-dimensional estimation of the electron density in the solar corona by tomographic inversion of k-coronagraph measurements," M.S. thesis, University of Illinois at Urbana-Champaign, 2004.

[59] M. Belge, M. E. Kilmer, and E. L. Miller, "Efficient determination of multiple regularization parameters in a generalized L-curve framework," *Inverse Problems*, vol. 18, no. 4, pp. 1161–1183, August 2002.

[60] B. Sharif, "Remote image formation from limited data: A hybrid technique, fundamental limitations, and optimal design," M.S. thesis, University of Illinois at Urbana-Champaign, 2004.

[61] S. Velamparambil, W. C. Chew, and J. Song, "10 million unknowns: Is it that big?" *IEEE Antennas and Propagation Magazine*, vol. 45, no. 2, pp. 43–58, April 2003.

[62] X. Zhang, "Ultrasound imaging for the early detection of breast tumors using conjugate gradient based solutions to the inverse problem," Ph.D. dissertation, Washington State University, 2000.

[63] M. A. Haun, D. L. Jones, and W. D. O'Brien, Jr., "Overdetermined least-squares aberration estimates using common-midpoint signals," *IEEE Transactions on Medical Imaging*, vol. 23, no. 10, pp. 1205–1220, October 2004.